



THE UNIVERSITY *of* EDINBURGH

Edinburgh Research Explorer

Gaseous CO₂ behaviour during water displacement in a sandstone core sample

Citation for published version:

Al-zaidi, E, Edlmann, K & Fan, X 2019, 'Gaseous CO₂ behaviour during water displacement in a sandstone core sample', *International Journal of Greenhouse Gas Control*, vol. 80, pp. 32-42.
<https://doi.org/10.1016/j.ijggc.2018.11.015>

Digital Object Identifier (DOI):

[10.1016/j.ijggc.2018.11.015](https://doi.org/10.1016/j.ijggc.2018.11.015)

Link:

[Link to publication record in Edinburgh Research Explorer](#)

Document Version:

Peer reviewed version

Published In:

International Journal of Greenhouse Gas Control

General rights

Copyright for the publications made accessible via the Edinburgh Research Explorer is retained by the author(s) and / or other copyright owners and it is a condition of accessing these publications that users recognise and abide by the legal requirements associated with these rights.

Take down policy

The University of Edinburgh has made every reasonable effort to ensure that Edinburgh Research Explorer content complies with UK legislation. If you believe that the public display of this file breaches copyright please contact openaccess@ed.ac.uk providing details, and we will remove access to the work immediately and investigate your claim.



Gaseous CO₂ Behaviour during Water Displacement in a Sandstone Core Sample

Ebraheam Al-Zaidi^a, Katriona Edlmann^b, Xianfeng Fan^{*a}

^aInstitute for Materials and Processes, School of Engineering, The King's Buildings, The University of Edinburgh, Mayfield Road, Edinburgh, EH9 3JL, United Kingdom

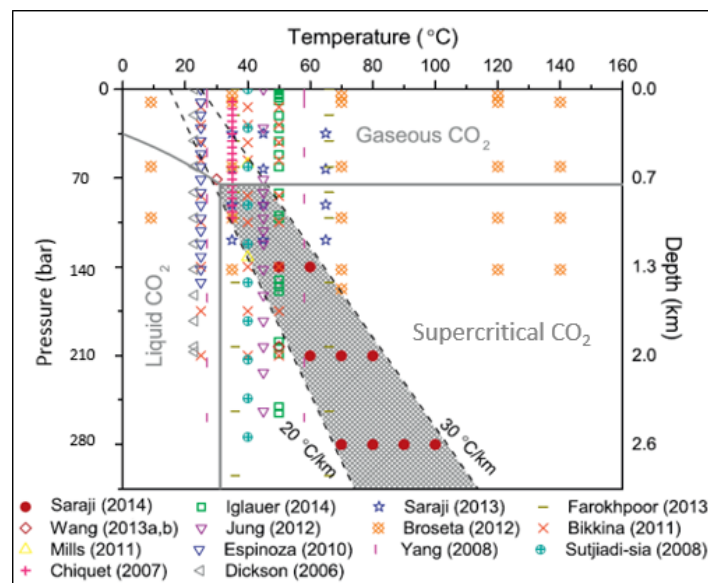
^bSchool of Geoscience, Grant Institute, The King's Buildings, The University of Edinburgh, James Hutton Road, Edinburgh EH9 3FE, United Kingdom.

* Corresponding author. Tel.: +44 0 131 6505678; fax: +44 0131 6506551. E-mail address: x.fan@ed.ac.uk

Abstract: CO₂ injection into subsurface formations involves the flow of CO₂ through a porous medium that also contains water. The injection, displacement, migration, storage capacity and security of CO₂ is controlled mainly by the interfacial interactions and capillary, viscous, and buoyancy forces which are directly influenced by changes in subsurface conditions of pressure and temperature; the impact of bouncy forces is assumed negligible during this study. In this study, gaseous CO₂ is injected into a water-saturated sandstone core sample to explore the impact of fluid pressure (40-70 bar), temperature (29-45 °C), and CO₂ injection rate (0.1-2 ml/min) on the dynamic pressure evolution and displacement efficiency. This study highlights the impact of capillary or viscous forces on the two-phase flow characteristics and shows the conditions where capillary or viscous forces become more influential. The results reveal a moderate to considerable impact of the parameters investigated on the differential pressure profile, endpoint CO₂ relative permeability ($K_{rCO_2}^{max}$), and irreducible water saturation (S_{wr}). Overall, the increase in fluid pressure, temperature, and CO₂ injection rate cause an increase in the maximum and final differential pressures, an increase in the $K_{rCO_2}^{max}$, a reduction in the S_{wr} . S_{wr} was in the range of around 0.38-0.45 while $K_{rCO_2}^{max}$ was less than 0.25. The data show a significant influence for the capillary forces on the pressure and production behaviour. The capillary forces produce high oscillations in the pressure and production data while the increase in viscous forces impedes the appearance of these oscillations. The appearance and frequency of the oscillations depend on the fluid pressure, temperature, and CO₂ injection rate but to different extents.

29 1 Introduction

30 Carbon capture and storage (CCS) is regarded as one of the most promising techniques that can
 31 deal effectively with the increasing emissions of anthropogenic CO₂ into the atmosphere due to fossil
 32 fuel burning and other human activities ([Bachu, 2001](#); [Hangx et al., 2013](#); [Kazemifar et al., 2015](#)). The
 33 captured CO₂ can be sequestered in deep saline aquifers, depleted or abandoned oil and gas reservoirs
 34 ([Delshad et al., 2010](#); [Gozalpour et al., 2005](#); [Kaveh et al., 2012](#)), or unmineable coal bed seams ([Kaveh](#)
 35 [et al., 2012](#); [Plug and Bruining, 2007](#)) to enhance recovery from hydrocarbon reservoirs, increase
 36 methane production from coal beds, or extract geothermal heat from subsurface formations ([Kaveh et](#)
 37 [al., 2012](#); [Tutolo et al., 2015](#)). Figure 1 presents a summary of the pressure and temperature ranges at
 38 which saline aquifers are found underground and highlights that CO₂ can exist in a gaseous, liquid or
 39 supercritical phase ([Bachu, 2000](#); [Espinoza and Santamarina, 2010](#); [Frailey et al.](#); [Nourpour Aghbash](#)
 40 [and Ahmadi](#); [Saraji et al., 2014](#); [Sohrabi et al.](#)).



41

42 Figure 1: The pressure and temperature ranges at which saline aquifers are found underground
 43 ([Saraji et al., 2014](#)). This study is conducted under pressure ranged from 40 to 70 bar and temperature
 44 ranged from 29 to 45 °C.

45 During CO₂ injection in subsurface formations, the bulk of the injected CO₂ (as a non-wetting fluid)
 46 will displace the formation water (as a wetting fluid) in an immiscible displacement ([Basbug et al., 2005](#);
 47 [Herring et al., 2014b](#)). The displacement of the injected CO₂ depends on a number of parameters,

48 namely, the interfacial interactions (e.g. interfacial tension and wettability), solubility of CO₂ in
49 formation water, densities and viscosities of fluids present, petrophysical properties of the subsurface
50 formation, injection rate and its duration , and more importantly on the capillary and viscous forces
51 ([Cinar and Riaz, 2014](#); [Duan and Sun, 2003](#); [Pentland et al., 2011b](#); [Trevisan et al., 2017](#)). The capillary
52 forces at the CO₂-water interface are of considerable importance in determining the nature of the flow
53 through pores ([Roof, 1970](#)). Any change in subsurface conditions of pressure and temperature will have
54 a significant impact on the interfacial interactions ([Espinoza and Santamarina, 2010](#); [Liu et al.](#); [Plug and](#)
55 [Bruining, 2007](#); [Yang et al., 2007](#)), the viscous forces due to the change in viscosity ([Bachu and Bennion,](#)
56 [2008b](#)) and the capillary forces. The change in interfacial interactions, and viscous and capillary forces
57 due to the change in underground conditions will have a considerable influence on the capillary
58 pressure, relative permeability ([Alkan et al., 2010](#)), pore-scale fluid distribution ([Al-Menhali and](#)
59 [Krevor, 2014](#)), CO₂ injection, fluid migration, capacity and long-term fate of CO₂ storage in saline
60 aquifers ([Levine et al., 2011](#); [Saraji et al., 2013](#); [Wang et al., 2015](#)), CO₂-enhanced oil and gas recovery
61 processes ([Gozalpour et al., 2005](#); [Qi et al., 2010](#)). According to Salimi et al., the change in capillary
62 pressure, due to the change in the operational conditions, can have a direct influence the CO₂-storage
63 capacity and the heat recovery due to its impact on the solubility and density of both CO₂ and water
64 ([Salimi et al., 2012](#)). Thus, it is of utmost importance to have a deep insight into the dynamic behaviour
65 of CO₂ under different operational conditions.

66
67 CO₂ has been used in the oil industry for a long time, in particular, to increase productivity through
68 Enhanced Oil Recovery (EOR), and extensive research has been undertaken describing multi-phase
69 flow properties of CO₂-oil systems ([Bahralolom et al., 1988](#)). On the other hand, much less laboratory
70 investigations have been done for CO₂-water (brine) systems ([Perrin and Benson, 2010](#)). Those
71 published have mainly focused on CO₂ wettability ([Al-Menhali and Krevor, 2014](#); [Bikkina, 2011](#);
72 [Farokhpoor et al., 2013a](#); [Kaveh et al., 2012](#); [Sakurovs and Lavrencic, 2011](#); [Saraji et al., 2013](#)), CO₂-water
73 (brine) interfacial tension ([Aggelopoulos et al., 2010](#); [Bachu and Bennion, 2008b, 2009](#); [Busch and](#)

74 [Müller, 2011](#); [Chiquet et al., 2007](#); [Li et al., 2012](#); [Yu et al., 2012](#)), relative permeability ([Bachu, 2013](#);
75 [Krevor et al., 2015](#); [Liu et al.](#); [Perrin et al., 2009](#)) and capillary pressure ([Busch and Müller, 2011](#); [Pini et](#)
76 [al., 2012](#); [Plug and Bruining, 2007](#)). Cinar and Riaz showed that much of the research has been directed
77 to investigate the fluid properties rather than studying the multiphase flow properties of the CO₂-water
78 systems ([Cinar and Riaz, 2014](#)).

79 The limited investigations of the multiphase flow characteristics of CO₂-water (brine) systems have
80 involved laboratory experiments ([Jobard et al., 2013](#)), computational modelling ([Jobard et al., 2013](#); [Ma](#)
81 [et al., 2013](#); [Xu et al., 2011](#)), and field scale projects ([Wang et al., 2015](#)). The CO₂-water (brine)
82 investigations included core flooding displacements performed at liquid, supercritical and gaseous CO₂
83 conditions. Current literature survey of the CO₂-water (brine) multiphase flow experiments showed
84 that most of these experiments were supercritical (Sc) CO₂-brine (water) displacements studies, which
85 were performed on various porous media such as core samples ([Berg et al., 2013](#); [Edlmann et al., 2013](#)),
86 micromodels ([Cao et al., 2016](#)), and packed beds of glass beads ([Song et al., 2012](#); [Suekane et al., 2005](#)).
87 In these studies related to supercritical CO₂ migration, researchers have examined various parameters
88 such as relative permeability curves ([Berg et al., 2013](#); [Chang et al., 2013](#); [Krevor et al., 2013](#); [Suekane et](#)
89 [al., 2005](#); [Suenaga and Nakagawa, 2011](#)), capillary pressure curves ([Herring et al., 2014a](#); [Wang et al.,](#)
90 [2013](#)), CO₂ residual saturation and distribution ([Alemu et al., 2011](#); [Chang et al., 2013](#); [Herring et al.,](#)
91 [2014a](#); [Pentland et al., 2011a](#); [Saeedi et al., 2011](#); [Suekane et al., 2005](#)), heterogeneity impact ([Ott et al.,](#)
92 [2015](#); [Perrin and Benson, 2010](#); [Shi et al., 2011](#); [Wang et al., 2013](#)), water displacement efficiency ([Cao et](#)
93 [al., 2016](#)), mass transfer ([Berg et al., 2013](#)), and formation dry-out ([Ott et al., 2011](#)). Some liquid (L) CO₂-
94 water (brine) core flooding displacements were conducted to investigate the multiphase flow
95 characteristics of CO₂-water-porous media ([Manceau et al., 2015](#)), CO₂ residual saturation and
96 distribution ([Alemu et al., 2011](#)), and pore-scale heterogeneity ([Zhang et al., 2011](#)).

97 On the other hand, very scarce data was found regarding gaseous (G) CO₂ injection into water
98 (brine) saturated porous systems ([Islam et al., 2013](#); [Jiang et al., 2017](#); [Lassen et al., 2015](#); [Yu et al., 2014](#)).

99 Even though liquid and supercritical CO₂ injection is more efficient, the dynamic behaviour of gaseous
100 CO₂ in reservoir rock is necessary information, particularly considering that many potential saline
101 storage aquifers are within temperature and pressure conditions of the gaseous CO₂ phase ([Figure 1](#))
102 and that any leakage of CO₂ from deeper storage would inevitably result in a phase change to a gaseous
103 CO₂ state ([Edlmann et al., 2016](#); [Miocic et al., 2016](#)). The existing GCO₂-water experiments were
104 designed to investigate the crossover zone of flow regimes, impact of capillary number, CO₂ injection
105 rates and permeability on displacement efficiency. Islam et al. conducted GCO₂-water experiments at 1
106 bar and 25 °C using a vertical Hele-Shaw cell filled with micro-beads to investigate the crossover zone
107 from capillary to viscous to fracture fingering. They observed that all the three fingering patterns can
108 occur in the cell but at different heights ([Islam et al., 2013](#)). Jiang et al. performed both immiscible and
109 miscible drainage GCO₂-water displacements inside a packed bed filled with quartz glass beads to have
110 a better understanding of the two-phase flow characteristics inside porous media. The experiments
111 were conducted at CO₂ injection rates varying from 0.01 to 3 ml/min and at 60 bar and 24.85 °C. They
112 observed that: (I) at low CO₂ injection rates, the CO₂ dissolution increases; (II) the increase in glass beads
113 diameter (i.e. higher permeability) leads to a decrease in the capillary forces ([Jiang et al., 2017](#)). Yu et al.
114 conducted immiscible drainage GCO₂-water displacements at 60 bar and 24.85 °C inside a packed bed
115 of glass beads (0.2 mm diameter) to study the impact of the capillary number on displacement
116 efficiency. They noticed that the increase in the capillary number, when it is between 10⁻¹¹ and 10⁻¹⁰,
117 results in a sharp reduction in the residual water saturation as a result of increasing the impact of the
118 viscous forces ([Yu et al., 2014](#)).

119 Despite the considerable research on the CO₂-water (brine) systems and its practical importance,
120 the analysis of the pressure data in core flooding has been widely overlooked ([Rezaei and Firoozabadi,](#)
121 [2014](#)). To the authors' best knowledge, there is no detailed investigation into the dynamic pressure
122 evolution and displacement efficiency of gaseous CO₂ during its injection into a water saturated core
123 sample. In this paper, laboratory dynamic drainage experiments were performed by injecting pure CO₂
124 into the deionised water-saturated sandstone core sample to investigate the impact of fluid pressure,

125 temperature, and CO₂ injection rate on the differential pressure profile, water production, and endpoint
126 effective and relative permeabilities of CO₂. This study also highlights the impact of capillary and
127 viscous forces on the pressure and production data as well as shows the conditions at which capillary
128 or viscous forces become more influential. During these dynamic displacements, the transient pressure
129 at the inlet and outlet sides of the core and the transient outflow rates of water and CO₂ were measured
130 and analyzed. The endpoint water saturations of CO₂ and water were also calculated.

131 **2 Materials**

132 A sandstone core sample from the Guillemot A Field in the North Sea was used to perform the
133 unsteady state GCO₂-water drainage experiments. The core sample has a diameter of 2.54 cm and a
134 length of 7.62 cm. The average porosity and absolute water permeability of the core sample were about
135 14% and 15.8 millidarcys, respectively. This study is one in a series, thus the core sample description,
136 the experimental setup and the CO₂-water displacement procedures can be seen in our recent
137 publication ([Al-Zaidi et al., 2018](#)).

138 **3 Results and discussion**

139 To gain a deep insight into the dynamic behaviour of GCO₂-water drainage displacements under
140 various fluid pressure, temperature, and injection rate conditions; the inlet and outlet pressure, CO₂
141 and water out flowrate, the irreducible water saturation and endpoint effective and relative
142 permeabilities of CO₂ were measured and analyzed.

143 In this study, the difference between the pressure transducer readings at the inlet and outlet sides
144 of the core sample has been used to calculate the differential pressure. The differential pressure during
145 horizontal CO₂ injection is largely influenced by the capillary and viscous forces. The capillary forces
146 are controlled mainly by the CO₂-water interfacial tension, contact angle (i.e. wetting status), pore
147 diameter and geometry ([Alkan et al., 2010](#); [Bikkina et al., 2016](#); [Chatzis and Morrow, 1984](#); [Fulcher Jr et al., 1985](#)). The wetting status plays an important role in determining the imbibition and the distribution
148 of the wetting and non-wetting phases inside the porous media ([Chalbaud et al., 2007](#); [Espinoza and](#)

150 [Santamarina, 2010](#)). The capillary forces, which are responsible for the entrapment of one phase by
 151 another during immiscible displacements in porous media ([Akbarabadi and Piri, 2013](#); [Chatzis and](#)
 152 [Morrow, 1984](#)), arise from the presence of the interface between the immiscible fluids ([Bikkina et al.,](#)
 153 [2016](#)) and significantly dominate the multiphase flow, especially in low permeability rocks and
 154 fractured reservoirs ([Schembre and Kovscek, 2003](#)). On the other hand, the viscous forces are controlled
 155 mainly by the viscosity of both displacing and displaced fluids, the fluid velocity in the pores, the
 156 amount of each fluid (i.e. saturation) in the pore, and the core sample properties (e.g. frontal area,
 157 permeability, and length). Espinoza and Santamarina ([Espinoza and Santamarina, 2010](#)) proposed the
 158 following equation to account for the impact of the capillary and viscous forces on the differential
 159 pressure as follow:

$$160 \quad \Delta P = P_{CO_2} - P_{water} = 4 \frac{\sigma_{CO_2-water} \cos\theta}{d} + v \frac{32L}{d^2} \left(\frac{l_{CO_2}\mu_{CO_2} + l_{water}\mu_{water}}{L} \right) \quad (1)$$

161 Where ΔP is the differential pressure across the core sample (Pa). P_{CO_2} and P_{water} are the pressures
 162 of CO₂ phase and water phase, respectively. $\sigma_{CO_2-water}$ is the CO₂-water interfacial tension (mN/m), θ the
 163 contact angle, d (m) the diameter of the largest effective pore ([Chiquet et al.](#); [Chiquet et al., 2007](#);
 164 [Farokhpoor et al., 2013b](#); [Han et al., 2010](#)), L (m) the length of the core sample, l (m) the length of CO₂
 165 or water phase inside the core sample, v (m/s) the fluid velocity in the pores, and μ (Pa·s) the viscosity
 166 of the fluids. The first term of Eq.1 refers to the Young-Laplace equation, which accounts for the
 167 capillary forces, while the second term refers to the Poiseuille's equation ([Espinoza and Santamarina,](#)
 168 [2010](#); [Li, 2015](#)), which account for the viscous forces. For small injection rate and high viscosity contrast
 169 conditions [the impact of viscous forces can be neglected](#), thus Eq.1 can be reduced to the Young-Laplace
 170 equation ([Li, 2015](#)) as follows:

$$171 \quad \Delta P = P_{CO_2} - P_{water} = 4 \frac{\sigma_{CO_2-water} \cos\theta}{d} \quad (2)$$

172 The Young-Laplace equation is used to determine the critical pressure point, which is the
 173 differential pressure required for the displacing fluid to enter the core sample for the first time. The

174 non-wetting fluid cannot enter the core sample unless its pressure becomes higher than the critical
175 pressure point ([Han et al., 2010](#)).

176 In this study, the experimental results have been categorized into two main sections. The first
177 section presents and discusses the impact of the experimental fluid pressure, temperature and CO₂
178 injection rate on the differential pressure profiles while the second section deals with the impact of the
179 parameters investigated on the endpoint CO₂ effective (relative) permeability and irreducible water
180 saturation.

181 It should be noted that during this study, the term low and high-fluid pressure refers to the
182 experiments conducted at pressures less and higher than 50 bar, respectively. The low and high
183 temperature refers to the experiments performed at less or higher than 33 °C, respectively. The low,
184 medium and high injection rates refer to the experiments performed at injection rate ranging from 0.1
185 to 0.2 ml/min, from 0.3 to 0.6 ml/min, and from 1 to 2 ml/min, in sequence. The corresponding time
186 refers to the time required to reach the maximum-differential pressure at the start of the experiment.
187 The quasi-differential pressure refers to the differential pressure at the end of the experiment.

188 ***3.1 Differential Pressure Profile of GCO₂-Water Drainage Displacements***

189 To investigate the effect of fluid pressure, experimental temperature, and CO₂ injection rate on the
190 differential pressures, series of GCO₂-water displacements were performed at various fluid pressures
191 (from 40 to 70 bar), experimental temperatures (29-45 °C) and CO₂ injection rates (0.1-2 ml/min).

192 ***3.1.1 Effect of Fluid Pressure on the Differential Pressure Profile of GCO₂-Water Drainage*** 193 ***Displacements***

194 [Figure 2](#) presents the impact of increasing fluid pressure on the differential pressure profile of
195 GCO₂-water drainage displacements. A number of trends are identifiable: Firstly, the differential
196 pressure profile at all fluid pressures is characterized by a high initial increase, immediately followed
197 by a steep rapid reduction and then followed by a quasi-differential pressure. Secondly, there are

198 multiple oscillations of these cycles. The frequency of these oscillating cycles increases as fluid pressure
199 increases along with a rise in the values of the maximum and quasi-differential pressures.

200 The high initial increase in the differential pressure can be related to the capillary pressure. The
201 following reduction in the differential pressure profile reflects the impact of the reduction in both
202 capillary forces and viscous forces according to Eq.1. The injection of gaseous CO₂ into the core sample
203 generates the initial increase in differential pressure to overcome the capillary entry pressure for the
204 invasion of the gaseous CO₂ ([Chang et al., 2013](#)). The reduction in the capillary forces can be associated
205 with the reduction in the pore resistance to CO₂-water interfaces as the number of pores opened by CO₂
206 is increased ([Kwelle, 2017](#)). This agrees very well with Kwelle's finding, who noticed a high reduction
207 in the differential pressure profile as the CO₂-water interface is displaced out of microcapillary tubes
208 ([Kwelle, 2017](#)). The reduction in the viscous forces can be related to the combined effect of the dynamic
209 change in relative permeability of gaseous CO₂ and water and the high rate replacement of a more
210 viscous fluid (water) with a less viscous fluid (CO₂) ([Chang et al., 2013](#)). [Replacing water by CO₂ at a](#)
211 [high rate](#) can be linked to (a) the high mobility ratio due to the high viscosity contrast and (b) gas
212 expansion effects which generate an increase in volumetric CO₂ injection rate inside the core sample.

213 • The gas expansion can, in turn, be related to the density change of the injected CO₂ due to the
214 temperature difference between inside the water bath (i.e. 29 to 45 °C depending on the experimental
215 conditions) and outside it (room temperature 18-20 °C). The density of the injected CO₂ varies as the
216 CO₂ enters the water bath dependant on the injection rate, fluid pressure and the temperature difference
217 from the pump to the sample. The density ratio (d_r) suggested by Perrin and Benson ([Perrin and Benson,](#)
218 [2010](#)) has been used to calculate the injection rate inside the core sample. For instance, at an
219 experimental pressure of 40 bar, an injection rate of 1 cm³/min at 20 °C becomes 1.7522 cm³/min at 33
220 °C. However, at an experimental pressure of 70 bar and the same injection rate and temperature
221 conditions, it becomes 5.281cm³/min.

$$222 \quad d_r = \frac{P_1 T_2 Z_2}{P_2 T_1 Z_1} \quad (3)$$

223

224 [Figure 2](#) reveals that the differential pressure profiles are characterized by multiple differential
225 pressure (PD) oscillations. The appearance of these PD oscillations can be related to the impact of the
226 capillary forces at the trailing end of each CO₂-water slug during CO₂ flooding ([Nutt, 1982](#)) or the
227 capillary end effects. According to Nutt, the impact of the capillary forces at the trailing end of the CO₂-
228 water slug is governed by the wetting status of the injected fluid. [If a non-wetting fluid \(e.g. CO₂\) is
229 injected, then the capillary forces will work in an opposite direction to the applied viscous forces. Thus,
230 as water depletion is progressed, the applied viscous forces will drop until they become less than the
231 capillary forces. Upon reaching this point, the flow of the non-depleted capillaries is potentially blocked
232 by the capillary forces \(\[Nutt, 1982\]\(#\)\). This blockage occurs due to a re-imbibition process of the wetting
233 phase inside the core sample, which was noticed by Hildenbrand et al \(\[Hildenbrand et al., 2002\]\(#\)\).](#)
234 Hildenbrand et al. observed that the re-imbibition process occurs when the excess pressure in the non-
235 wetting phase declines after the gas breakthrough ([Hildenbrand et al., 2002](#)), as shown in [Figure 3](#). This
236 re-imbibition process occurs in a progressive manner starting with the smallest pores and continuing
237 to the larger pores, leading to the successive loss of the interconnected flow-paths, which, in turn, leads
238 to a progressive decline in the non-wetting phase relative permeability. Finally, when the last
239 interconnected flow-path for the non-wetting phase is blocked, the permeability of the non-wetting
240 phase will drop to zero ([Hildenbrand et al., 2002](#)). According to Hildenbrand et al., this re-imbition
241 process can result in a residual water saturation when certain-gas filled pores become isolated a result
242 of interrupting the flow pathways. The maximum differential pressure required to open the flow paths
243 again can be used to determine the largest effective pore radius and, hence, the sealing efficiency of the
244 rock ([Hildenbrand et al., 2002](#)).

245 Therefore, since our core sample is water-wet, the pressure of the injected CO₂ had to build up to
246 a certain level to overcome the capillary forces that blocked the CO₂ outflow rate ([Nutt, 1982](#)). Due to
247 the high compressibility nature of the gaseous CO₂, the injected CO₂ will accumulate inside the core

248 sample and the connections pipes until the differential pressure becomes high enough to overcome the
249 capillary forces. Once the blocked capillaries are opened to flow, the cumulative CO₂ will expel the
250 liquid drops that block the pores out of the core sample quickly; the rate of **expulsion** is expected to
251 increase with the fluid pressure. The development of this phenomenon is highly influenced by the core
252 sample properties and the injection rate due to their direct impact on viscous and capillary forces. As a
253 result, this phenomenon is expected to be reduced when the injection rate, i.e. viscous pressure drop,
254 becomes high enough to overcome the capillary forces ([Nutt, 1982](#)). However, due to the cyclic
255 reduction of the viscous pressure drop (i.e. viscous forces) to the level that becomes insufficient to
256 overcome the capillary forces, this phenomenon of oscillations can occur frequently.

257 On the other hand, since the GCO₂-water displacements are strongly influenced by the capillary
258 end effects and viscous instabilities ([Müller, 2011](#)), it might be suggested that the appearance of the
259 oscillations is due to the impact of capillary end effects. The capillary end effects occur at both inlet and
260 outlet faces of the core sample, but its impact becomes more severe at the outlet face. According to
261 Müller, the capillary end effects can never be entirely prevented but can be corrected for ([Müller, 2011](#)).
262 The impact of capillary end effects and viscous instabilities can be reduced when the following scaling
263 coefficient proposed by Rapoport and Leas for stabilized floods becomes greater than one.

$$264 \quad Lu\mu \geq 1 \quad (4)$$

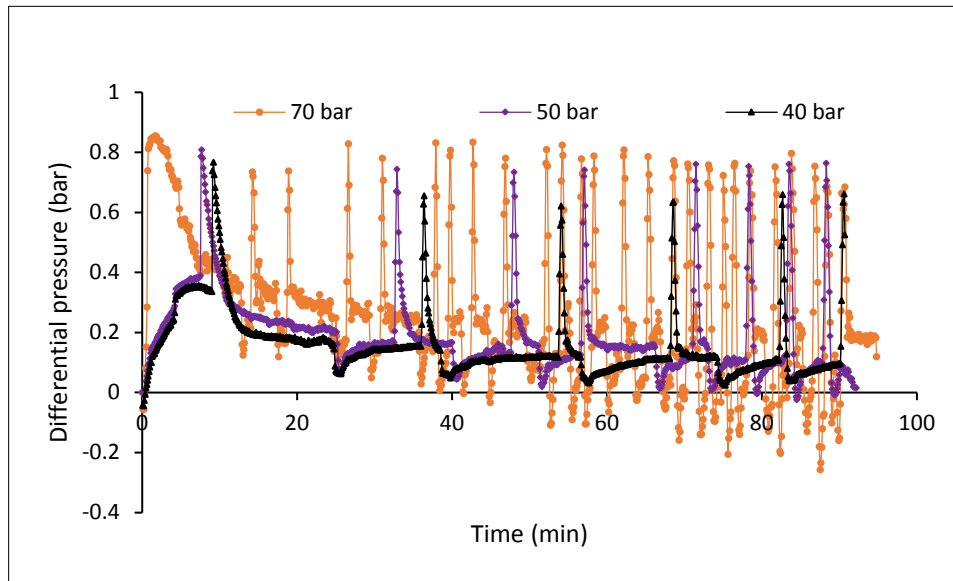
265 where L is the length of the medium (cm), u the Darcy velocity (cm/min), and μ the displacing
266 phase viscosity (cp) ([Fathollahi and Rostami, 2015](#)). The scaling coefficients for the 40, 50, and 70 bar
267 displacements are 0.0773, 0.0844, and 0.285, respectively. The scaling coefficients increased significantly
268 as the fluid pressure increased from 40 and 50 bar to 70 bar, which indicates a reduction in the impact
269 of capillary end effects with increasing fluid pressure. However, since the data from [Figure 2](#) reveal an
270 increase in the frequency of the oscillations with increasing fluid pressure, this indicates that the
271 capillary end effects are not responsible for the PD oscillation phenomenon. In addition, the

272 disappearance of the oscillations at lower injection rates as shown in [Figure 7](#) further supports the idea
273 that the oscillations are not because of the capillary end effects.

274 [Figure 2](#) also shows that increasing fluid pressure leads to an increase in the rate of the differential
275 pressure (PD) oscillations along with increases in the values of the maximum and quasi-differential
276 pressures and a reduction in the corresponding time (the time required to reach the maximum-
277 differential pressure at the start of the experiment). For illustration, it can be seen that as the fluid
278 pressure increased from 40 to 50 bar, the rate of the PD oscillations increased by around 33% and the
279 maximum-differential pressure increased by about 2.50%. The quasi-differential pressure was constant
280 at around 1 bar. The corresponding time declined by approximately 17%. However, as the fluid
281 pressure increased from 50 to 70 bar, the PD oscillations substantially increased by 225%, the maximum-
282 differential pressure raised by around 9% and the quasi-differential pressure increased by 165%. The
283 corresponding time dropped considerably by around 78%. The high reduction in the corresponding
284 time with increasing fluid pressure can be related mainly to the increase in gaseous CO₂ density and
285 the injection rate inside the core sample due to the expansion effects. [As gaseous CO₂ becomes denser,](#)
286 [it requires lesser time to be compressed to the required pressure.](#)

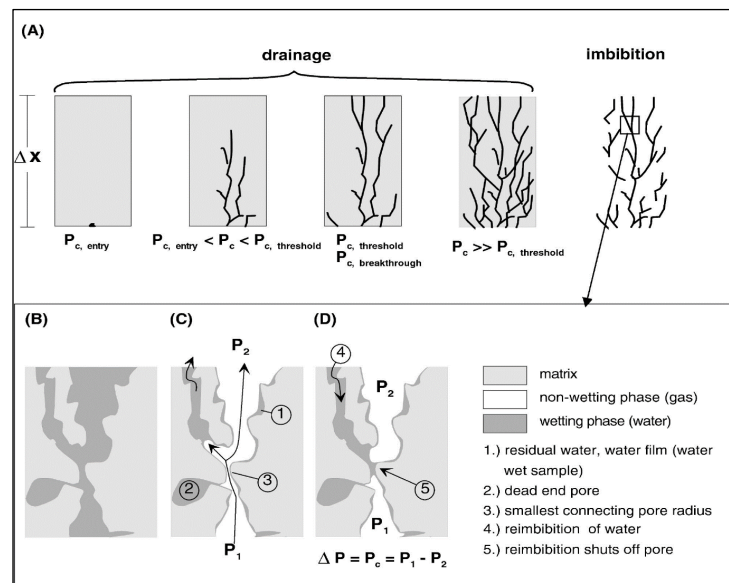
287 The increase in the maximum and quasi-differential pressures with increasing fluid pressure can
288 be related mainly to the magnitudes of both viscous and capillary forces. [According to Eq.1, as the fluid](#)
289 [pressure increases the viscous forces increase \[due to the increase in CO₂ viscosity and the injection rate](#)
290 [inside the core sample due to expansion impact\], while the capillary forces decrease \[because of the](#)
291 [reduction in the CO₂-water interfacial tension \(IFT\) \(\[Georgiadis et al., 2010\]\(#\)\) and the increase in the](#)
292 [contact angle \(\[Banerjee et al., 2013\]\(#\)\) due to increasing CO₂ solubility \(\[Bennion and Bachu; Yang et al.,\]\(#\)](#)
293 [2007\)\]. Thus, the increase observed in the differential pressures is the net result of the increase in the](#)
294 [viscous forces and the reduction in the capillary forces. Reducing capillary forces with increasing](#)
295 [pressure is expected to cause a reduction in the extent of differential pressure increase.](#)

296 The increase in the PD oscillations means the frequency of liquid drops expelled out of the core
 297 sample is increased. This can be associated mainly with the reduction in the capillary forces and the
 298 increase in gas density with increasing pressure. Increasing the gas density and reducing capillary
 299 forces mean less time was required to reach a differential pressure value which was sufficient to
 300 overcome the capillary forces; thus, increasing the frequency of the PD oscillations.



301

302 **Figure 2:** Effect of fluid pressure on the differential pressure profile of GCO₂-water displacements
 303 conducted at 0.4 ml/min and 33 °C.



304

305 **Figure 3:** Re-imbibition process in fine-grained rocks (schematic re-imbibition); (A) drainage, (B)
 306 initially water-saturated sample, (C) gas breakthrough, (D) re-imbibition ([Hildenbrand et al., 2002](#)).

307

3.1.2 Effect of Temperature on the Differential Pressure Profile of GCO₂-Water Displacements

Figure 4 presents the impact of increasing experimental temperature on the differential pressure profile. The results demonstrate that the increase in the experimental temperature has a significant impact on the differential pressure profile. Firstly, increasing the temperature increases the frequency of the PD oscillations. At an experimental temperature of 29 °C, the differential pressure profile experienced no oscillations. However, as the temperature increased to 31 °C, the oscillations appeared for the first time. A further increase in the temperature to 33 °C caused the number of oscillations to increase by double. Secondly, the increase in the temperature prompts an increase in the magnitude of the maximum-differential pressure. The quasi-differential pressure was almost constant due to the slight impact of both capillary forces and viscous forces at the end of core flooding.

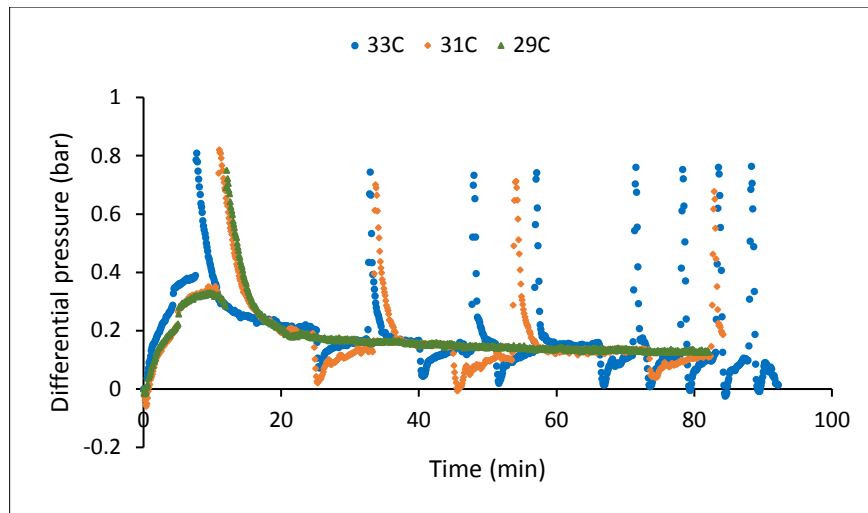
The appearance and frequency of the PD cycles with increasing temperature have three potential explanations. The first potential reason behind the onset of the oscillations and their frequency is the increase in the capillary forces despite the slight increase in viscous forces under these conditions. The increase in temperature leads to an increase in the CO₂-water IFT ([Iglauer et al., 2012](#)) with a reduction in the contact angle ([Yang et al., 2007](#)) due to the decline in the CO₂ solubility ([Bennion and Bachu; Yang et al., 2007](#)) as well as a slight increase in CO₂ viscosity, and a slight increase in CO₂ injection rate inside the core sample due to expansion effect. For illustration, as the experimental temperature increased from 29 to 31 °C, CO₂-water IFT increases from to 42.9 to 44.42 mN/m, CO₂ viscosity increases very slightly from 16.72 to 16.755 × [10⁻⁶(Pa·s)] and CO₂ injection inside the core sample increased from around 0.45 to 0.46 ml/min. However, a further increase in the experimental temperature to 33 °C caused the CO₂-water IFT to decrease to 34.1 mN/m ([Bachu and Bennion, 2008a](#)), CO₂ viscosity to increase to 16.805 × [10⁻⁶(Pa·s)] and CO₂ injection to increase to 0.466 ml/min.

The second possible reason might be related to the fluctuating behaviour in the CO₂-water IFT when the experimental temperature is around the critical point ([Bennion and Bachu](#)), as shown in [Figure 5](#). The third potential reason is that the PD oscillations might occur because of increasing

334 temperature which results in a quicker increase in the movement of CO₂ molecules. This is because each
335 individual molecule has more energy as it becomes hotter, according to the Kinetic molecular theory
336 ([Physics, 2017](#)). A high energetic CO₂ molecule might open the closed flow path, due to the increase in
337 capillary forces, quicker.

338 The results indicate that for the sandstone core sample (from the Guillemot A field, North Sea)
339 used in the experiment and under the aforementioned experimental conditions, the onset temperature
340 point of the oscillations is around 31 °C. The characteristics of the sandstone sample, e.g. pore size
341 distribution, play a key role in the onset of the PD oscillations phenomena as they have a direct
342 influence on the magnitude of the capillary forces as illustrated by Young-Laplace law (Eq.2).

343 The data also reveals that as the experimental temperature increased from 29 to 31 °C, the
344 maximum-differential pressure increased by around 12.5% (from 0.72 to 0.81 bar) and the
345 corresponding time dropped by around 9.1% (from 12.1 to 11 min). However, increasing the
346 temperature from 31 to 33 °C caused the differential pressure to decline slightly by 1.23% (from 0.82 to
347 0.81 bar) and the corresponding time dropped by 30% (from 11 to 7.7 min). The increase and decrease
348 in the maximum-differential pressure can be related mainly to the increase or decrease in the capillary
349 forces due to CO₂-water IFT, as stated above. [The highest reduction in the corresponding time occurred
350 as the temperature increased to 33 °C. This can be related to the highest reduction in the CO₂-water IFT
351 \(\[Bennion and Bachu\]\(#\)\), as shown in Figure 5.](#)

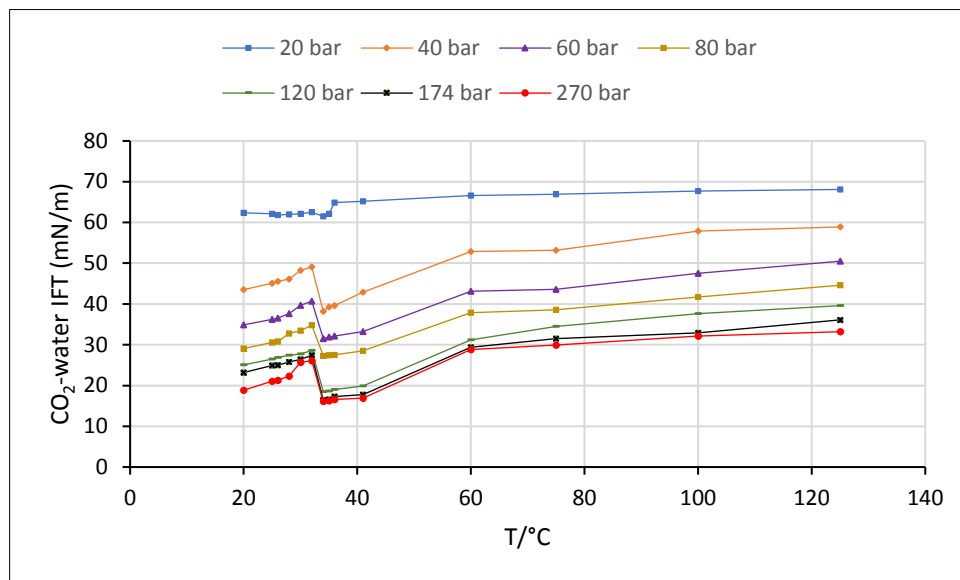


352

353

354

Figure 4: Effect of temperature on the differential pressure profile of GCO₂-water displacements conducted at 50 bar and 0.4 ml/min.



355

356

Figure 5: Interfacial tension for CO₂-Pure Water Systems adopted from ([Bachu and Bennion, 2008b](#)).

357

358

359

To further investigate the effect of the temperature on the differential pressure profile, and especially on the PD oscillations, additional GCO₂-water displacement experiments were conducted under a high-pressure of 70 bar and higher temperature conditions.

360

361

362

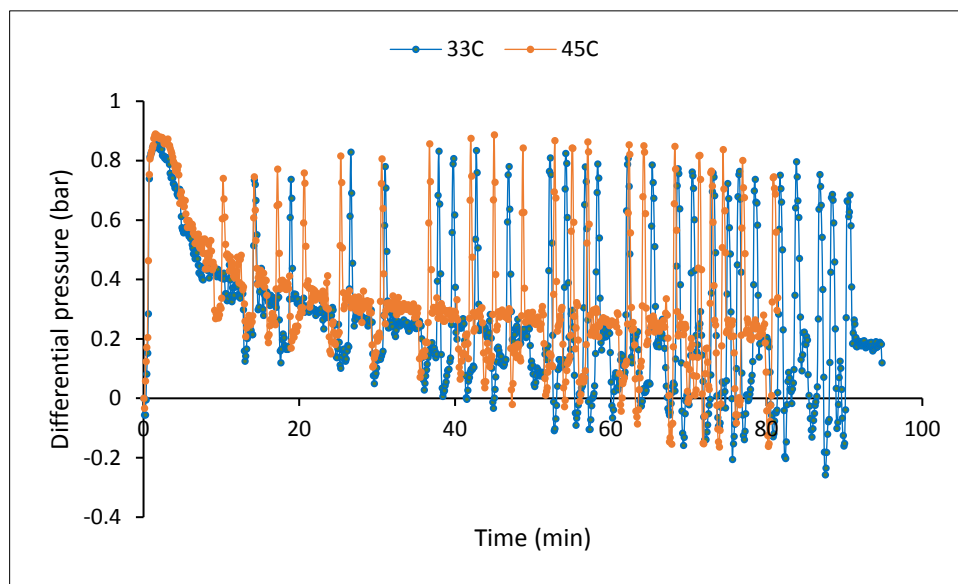
363

The data from Figure 6 shows that increasing the experimental temperature by 12 degrees (from 33 to 45 °C) at a high-pressure caused no further increase in the rate of the PD oscillations. Yet, it instigated a very slight increase in the maximum and quasi-differential pressures with a small reduction in the corresponding time. The maximum differential pressure increased by only 4.2% (from 0.854 to

364 0.89 bar) and the quasi-differential pressure by 4.81% (from 0.208 to 0.218 bar). The corresponding time
365 declined by around 17% (from 1.8 to 1.5 min).

366 The data showed no further increase in the PD oscillations occurred when there are no fluctuations
367 in the IFT as the temperature increased from 33 to 45 °C, as shown in [Figure 5](#). This suggests that the
368 IFT fluctuations might have highly influenced the frequency of PD oscillations.

369 The increase in the maximum and quasi-differential pressures can be related to the increase in the
370 capillary forces (because of the increasing CO₂-water interfacial tension and the reducing contact angle
371 ([Yang et al., 2007](#))), and the slight increase in the viscous forces (because of the increasing injection rate).
372 The magnitude of the viscous forces might have slightly declined because of the slight reduction in CO₂
373 viscosity with increasing temperature. For illustration, as the experimental temperature increased from
374 33 to 45 °C, the CO₂-water IFT increases from around 29.15 to around 33.4 mN/m ([Bennion and Bachu](#)),
375 and the CO₂ injection rate inside the core sample increased from 1.315 to 1.748 ml/min but the viscosity
376 decreases from 20.743 to 19.05 × [10⁻⁶(Pa·s)].



377

378 [Figure 6](#): Effect of temperature on the differential pressure profile of GCO₂-water displacements
379 conducted at 70 bar and 0.4 ml/min.

380 **3.1.3 Effect of CO₂ Injection Rate on the Differential Pressure Profile of GCO₂-Water Core**
381 **Floodings**

382 Figure 7, Figure 8 and Figure 9 show the impact of increasing CO₂ injection rate on the differential
383 pressure profile. For Figure 8, the experiments conducted at higher injection rate (2 ml/min) lasted
384 shorter than those conducted at lower injection rate (1 ml/min) to explore the impact of injection
385 volumes on the displacement efficiency. The results reveal that increasing the injection rate has a
386 significant impact on the differential pressure profile, mainly at early stages of core flooding. The data
387 reveal a number of important observations (A-E).

388 **A)** The data show that the higher the injection rate, the higher the maximum differential pressure
389 is. However, increasing the injection rate caused a slight increase in the quasi-differential pressure; the
390 corresponding time decreased at low injection rates and increased at high injection rates. For
391 illustration, as the CO₂ injection rate increased from 0.1 to 0.2 ml/min, the maximum-differential
392 pressure increased by 33.54% (from 0.161 to 0.215 bar), and the quasi-differential pressure by 5.88%
393 (from 0.068 to 0.072 bar) while the corresponding time reduced by almost half (from 13.5 to 6.5 min).
394 However, as the CO₂ injection rate increased from 1 to 2 ml/min, the maximum-differential pressure
395 increased by around 44% (from 0.833 to 1.201 bar), the quasi-differential pressure increased by around
396 15% (from 0.254 to 0.291 bar), and the corresponding time increased by 12% (from 3.3 to 3.7 min). The
397 increase in the corresponding time at high injection rates despite the increase in the CO₂ injection rate
398 can be related to the high increase in the magnitude of the maximum-differential pressure as well as
399 the low-density nature of the gaseous CO₂. Since the injected gaseous CO₂ was at low pressure (40 bar),
400 it needed a longer time to reach the higher maximum-differential pressure of 1.201 bar during the 2
401 ml/min-displacement.

402 **B)** The data from Figure 7 and Figure 8 reveals that as the injection rate increased by tenfold (from
403 0.1 to 1 ml/min, and from 0.2 to 2 ml/min), the quasi-differential pressure increased by only around
404 fourfold, (from 0.068 to 0.254 bar, and from 0.072 to 0.291 bar). This might be related to a potential

405 increase in the relative permeability with increasing injection rate ([Akbarabadi and Piri; Chang et al.,](#)
406 [2013](#)) that leads to a reduction in the viscous pressure drop.

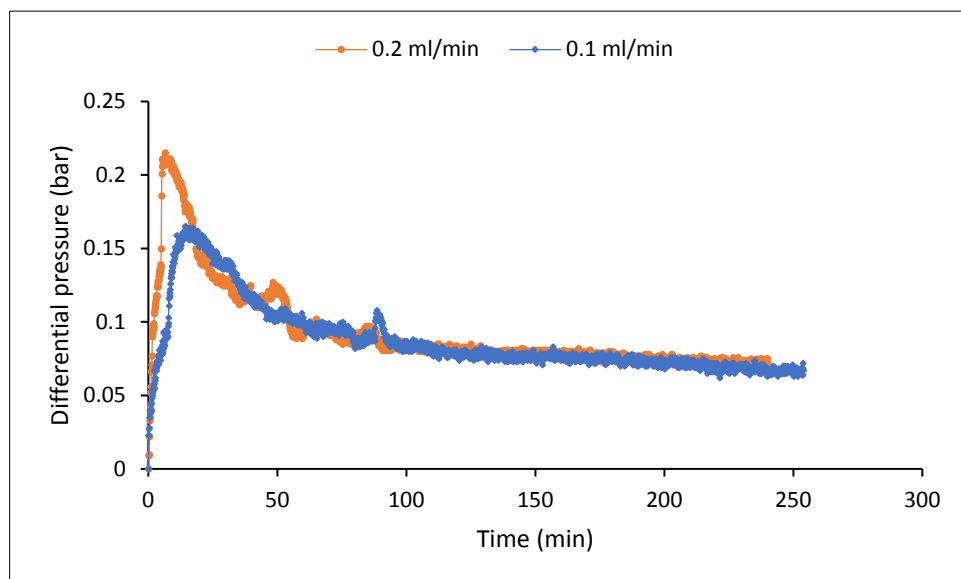
407 C) The data previously shown in [Figure 2](#) reveals that the differential pressure profile of the 40
408 bar-experiments is characterized by PD oscillations at 0.4 ml/min CO₂ injection rate. Surprisingly, the
409 data from [Figure 7](#) and [Figure 8](#) reveal no PD oscillations at lower and higher CO₂ injection rates. The
410 disappearance of the PD oscillations at higher injection rates (e.g. 1-2 ml/min) can be related to the high
411 increase in the pressure drop due to viscous forces. Thus, the viscous forces impeded the capillary
412 forces, which are responsible for the observed PD oscillations phenomenon ([Nutt, 1982](#)). On the other
413 hand, at lower CO₂ injection rates (e.g. 0.1 to 0.2 ml/min), CO₂ might flow through preferential inlet and
414 outlet pores ([Gunde et al., 2010](#)) that are characterized by low resistance to flow and by less capillary
415 forces. Consequently, CO₂ does not need to pass through the smallest channels that are characterized
416 by higher resistance to CO₂ flow and higher capillary forces, hence avoiding the impact of the capillary
417 forces that cause the oscillations.

418 D) To look in detail at the unexpected results regarding the appearance and disappearance of the
419 PD oscillations and the impact of CO₂ injection rate on the differential pressure profile, further
420 experiments were conducted at 40 bar [and](#) over a more detailed range of injection rates, as shown in
421 [Figure 9](#). It should be noted that the 0.4 ml/min GCO₂-water displacement is repeated to make sure that
422 the observations were not an experimental error.

423 The results from [Figure 9](#) show clearly that the PD oscillations occurred only at 0.4 ml/min for the
424 experiments conducted at a low pressure of 40 bar. Overall, the data confirm that the increase in the
425 injection rate produces an increase in the maximum-differential pressure and a reduction in its
426 corresponding time for this range of injection rates. The quasi-differential pressure reduced slightly
427 due to the potential increase in the relative permeabilities ([Akbarabadi and Piri; Chang et al., 2013](#)).

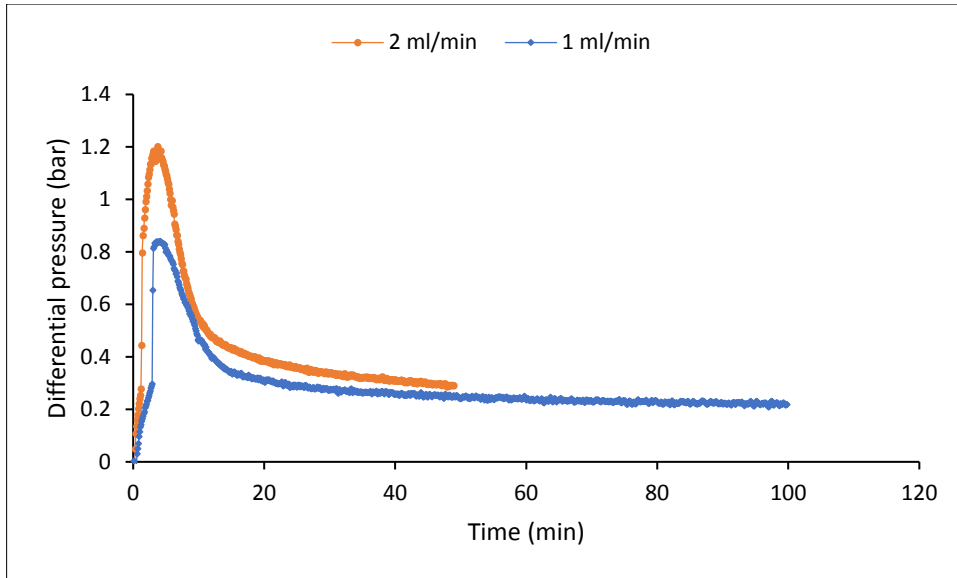
428 The data from [Figure 9](#) can be divided into two groups. The first group includes the experiments
429 conducted at a CO₂ injection rate of 0.3 and 0.4 ml/min while the second group involves the experiments

430 performed at 0.5 and 0.6 ml/min. As the CO₂ injection rate increased for the first lower injection rate
431 group, the maximum-differential pressure was almost constant at around 0.76 bar, but the
432 corresponding time reduced by 25% (from around 20 to 15 min). The second higher injection rate group
433 is characterized by a constant maximum-differential pressure of 0.938 bar and a constant corresponding
434 time of 6.5 min. Thus, the data reveals that shifting the CO₂ injection rate to the second group caused
435 the maximum-differential pressure to increase by 23.42% and the corresponding time to reduce by
436 around 57%. The increase in the maximum-differential pressure associated with shifting the CO₂
437 injection rate might be related to the properties of the core sample. It might have occurred because as
438 the injection rate increased from the first to the second group, the maximum-differential pressure had
439 to further increase to open new preferential flow paths for the injected CO₂ (Gunde et al., 2010). The
440 nearly constant maximum-differential pressure for each group might indicate a minimal impact for the
441 viscous forces on the differential pressure at low pressures. It indicates also that the expected increase
442 in the maximum-differential pressure due to increasing injection rate is reduced by the potential
443 increase in the relative permeability due to the increasing injection rate (Akbarabadi and Piri; Chang et
444 al., 2013).



445

446 **Figure 7:** Effect of CO₂ injection rate on the differential pressure profile of GCO₂-water
447 displacements conducted at 40 bar and 33 °C.

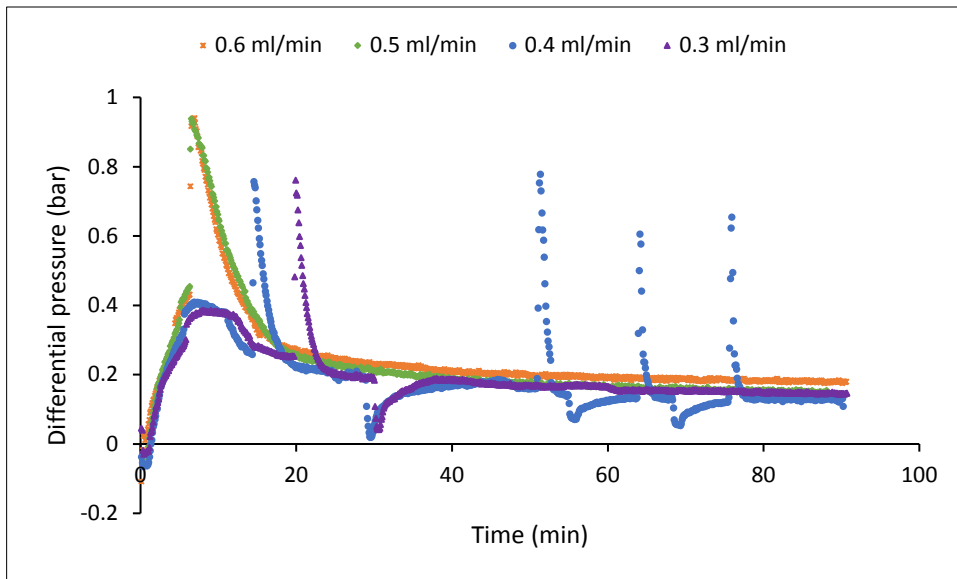


448

449

450

Figure 8: Effect of CO₂ injection rate on the differential pressure profile of GCO₂-water displacements conducted at 40 bar and 33 °C.



451

452

453

Figure 9: Effect of CO₂ injection rate on the differential pressure profile of GCO₂-water displacements conducted at 40 bar and 33 °C.

454

455

456

457

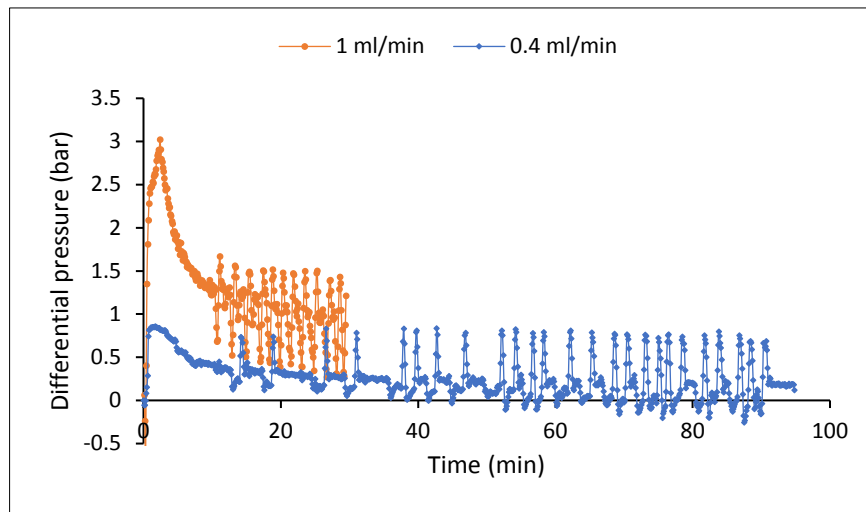
E) To further investigate the effect of CO₂ injection rate on the differential pressure profile and the phenomenon of the PD oscillations particularly, a second set of GCO₂-water displacements have been performed at a higher pressure (70 bar). To enable a clear comparison, the data was presented in two figures: Figure 10 and Figure 11.

458 E.1) The data shows clearly that conducting GCO₂-water displacements at higher pressure (70 bar)
459 caused the PD oscillations to appear over a wider range of CO₂ injection rates (from 0.2 to 1 ml/min). It
460 reveals also that the change in the maximum and quasi-differential pressures, corresponding time and
461 PD oscillations depend on the range of the injection rate; the highest change occurred as the injection
462 rate increased from 0.4 to 1 ml/min. For illustration, as the CO₂ injection rate increased from 0.4 to 1
463 ml/min, the maximum-differential pressure increased considerably by around 258% (from 0.845 to
464 3.024 bar) and the quasi-differential pressure increased by around 224.5% (from 0.265 to 0.86 bar). The
465 corresponding time prolonged by 140% (from 1 to 2.4 min), despite the increase in the injection rate,
466 due to the increase in the maximum-differential pressure. The frequency of the PD oscillations was
467 almost constant for the last 20 min of both experiments. The increase in the maximum and quasi-
468 differential pressures can be attributed to the increase in the viscous forces; the increase in the
469 corresponding time can be related to the high increase in the magnitude of the maximum differential
470 pressure.

471 E.2) On the other hand, as the CO₂ injection rate increased from 0.2 to 0.4 ml/min, the maximum-
472 differential pressure was almost constant at around 0.85 bar, the quasi-differential pressure slightly
473 increased, the corresponding time slightly reduced, and the frequency of the PD oscillations
474 considerably decreased but the magnitude of the PD oscillations significantly increased from around
475 0.25 to 0.825 bar. The nearly constant maximum-differential pressure (0.85 bar) at the low injection rates
476 (0.2 to 0.4 ml/min)-core floodings reveals a negligible impact of the viscous forces on the differential
477 pressure at the conditions investigated. However, the reduction in the frequency of the PD oscillations
478 might be attributed to CO₂ flow through preferential flow paths ([Gunde et al., 2010](#)).

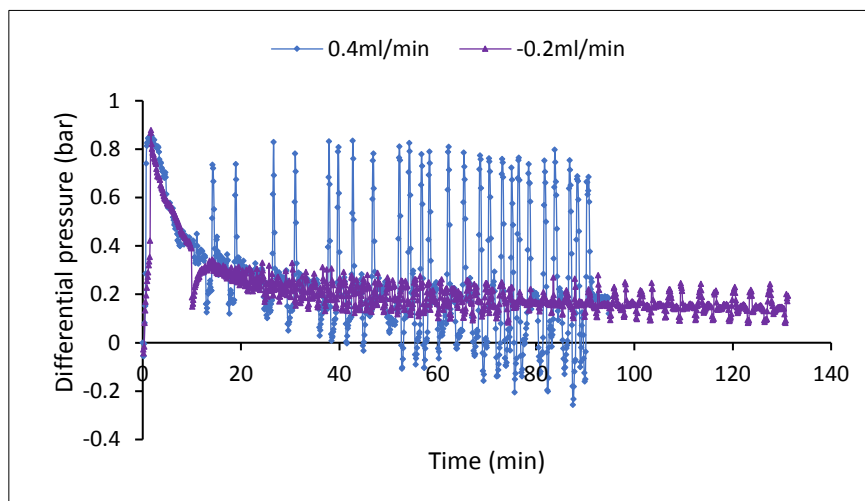
479 The frequency of the PD oscillations might depend to a considerable extent on the core sample
480 properties, the change in CO₂ distribution due to the change in the CO₂ injection rate, and the
481 operational conditions. For illustration, as the CO₂ injection rate increased from 0.2 to 0.4 ml/min, the
482 CO₂ might have distributed over a wider range of capillaries. Consequently, as the viscous pressure
483 drop declined because of water depletion, the CO₂ flow inside the smaller capillaries was blocked due

484 to their higher resistance to CO₂ flow. Later, as the pressure drop continued, the CO₂ flow in larger
485 capillaries was blocked, too. Ultimately, it came to the point when all capillaries were blocked by the
486 capillary forces ([Hildenbrand et al., 2002](#); [Nutt, 1982](#)). Thus, the increase in CO₂ distribution with
487 increasing injection rate might have led to prolonging the time required for the capillary forces to block
488 the CO₂ production from all opened interconnected flow paths. As a result, since the volume of the
489 opened capillaries were larger with increasing injection rate from 0.2 to 0.4 ml/min; therefore, the
490 frequency of the PD oscillations was reduced.



491

492 **Figure 10:** Effect of CO₂ injection rate on the differential pressure profile of GCO₂-water displacements
493 conducted at 70 bar and 33 °C.



494

495 **Figure 11:** Effect of CO₂ injection rate on the differential pressure profile of GCO₂-water
496 displacements conducted at 70 bar and 33 °C.

497 In summary, fluid pressure, temperature and CO₂ injection rate exert significant influences on the
498 differential pressure profile of the GCO₂-water drainage displacements. The differential pressure
499 profile at all fluid pressures, temperatures and injection rates is characterized by a high initial increase
500 immediately followed by a steep rapid pressure reduction and then by a quasi-pressure drop.

501 The differential pressure is controlled by the interplay of both capillary and viscous forces. The
502 increase in capillary forces leads to the appearance of the PD oscillations (the onset points) while the
503 increase in viscous forces causes their impedance.

504 There are multiple cycles of these oscillations and the occurrence and frequency of these
505 oscillations vary with fluid pressure, temperature and injection rate. The frequency of these oscillating
506 cycles increases as fluid pressure and fluid temperature increase but vary with injection rate and seem
507 to be fluid pressure dependent. These oscillations occurred only at 0.4 ml/min at low pressures (i.e. 40
508 bar), but they appeared over a wider range of injection rates at higher pressures (i.e. 70 bar). The
509 maximum-differential pressure reached during each cycle increases with increasing fluid pressure,
510 temperature and injection rate.

511 ***3.2 Effect of Fluid Pressure, Temperature, and Injection Rate on Irreducible Water*** 512 ***Saturation and Endpoint Effective and Relative Permeabilities of CO₂***

513 The effective and relative permeabilities of CO₂ are significantly important to the determination of
514 the efficiency and integrity of CO₂ sequestration in subsurface formations ([Busch and Müller, 2011](#);
515 [Rathnaweera et al., 2015](#)). At the end of the flooding experiment, the volume of the water produced
516 was measured, and the irreducible water saturation was calculated. Then, the core sample was weighed
517 to confirm the irreducible water saturation calculations. To calculate the endpoint effective (relative)
518 CO₂ permeability using Darcy's law, the average quasi-differential pressure and the average CO₂
519 outflow rate of the last period were used ([Akbarabadi and Piri; Chang et al., 2013](#)). The CO₂ viscosity
520 at the experimental pressure and temperature was calculated using the Peace software website ([Peace](#)
521 [software, 2017](#)).

522 The results from [Table 1](#) shows that both endpoint CO₂ relative permeability ($K_{rCO_2}^{max}$) ([Armstrong](#)
523 [et al., 2017](#)) and irreducible water saturation (S_{wr}) are dependent on the experimental conditions at
524 which they are measured. The S_{wr} was in the range of around 0.38-0.45 while the $K_{rCO_2}^{max}$ was less than
525 0.25. Busch and Müller obtained a low relative permeability for CO₂, too ([Busch and Müller, 2011](#)). Such

526 low relative permeability would tend to decrease injectivity while increasing displacements efficiency
527 ([Levine et al., 2011](#)).

528 The results from [Table 1](#) reveal that in general the increase in fluid pressure, temperature, and
529 injection rate lead to an increase in the $K_{rCO_2}^{max}$ and a decline in the S_{wr} . In case of increasing fluid
530 pressure and temperature, the high increase in the K_{rCO_2} can be attributed mainly to the high increase
531 in the injection rate inside the core sample due to the high impact of gas expansion ([Rostami et al., 2010](#);
532 [Skauge et al.](#)). This increase in volumetric CO₂ injection rate might result in forcing the CO₂ to flow
533 through a wider range of the core sample pores.

534 The displacements efficiency is controlled by many factors that include relative permeability,
535 wetting conditions, viscous fingering, gravity segregation, channelling, the amount of crossflow/mass
536 transfer ([Chukwudeme and Hamouda, 2009](#)), mobility ratio, and capillary number ([Kazemifar et al.,](#)
537 [2015](#)). The capillary number (Ca) refers to the ratio of the viscous forces to capillary forces ([Lenormand](#)
538 [et al., 1988](#)). The mobility ratio (M) refers to the ratio of the displaced to the displacing phase viscosities.
539 Increasing the contrast between the viscosity of the displacing and displaced fluid leads to a higher M
540 which will result in a more unstable configuration front. The following formulas are used to define
541 them:

$$542 \quad Ca = \frac{\mu_2 V_2}{\sigma \cos \theta} \quad (5)$$

$$543 \quad M = \frac{\mu_2}{\mu_1} \quad (6)$$

544 where μ is the dynamic viscosity, σ the interfacial tension between the displaced and the displacing
545 phases, 1 the subscript of the displaced phase, 2 the subscript of the displacing phase, θ the contact
546 angle between the two fluids and the surface, and V_2 the bulk velocity of the displacing fluid. The
547 flowing equation is used to define the bulk velocity.

$$548 \quad V_{bulk} = \frac{Q}{A \phi} \quad (7)$$

549 where Q is the volumetric injection rate, A the area of the frontal face of the core sample, and ϕ the
550 core sample porosity ([Kazemifar et al., 2015](#)). Based on the magnitudes of the Ca and the M , three
551 different regimes can be defined ([Kazemifar et al., 2015](#)). For the GCO₂-water displacement investigated
552 both Ca and M are small, which suggest a capillary fingering regime.

553 The reduction observed in the S_{wr} can be attributed mainly to the increase in the Ca and the
554 reduction in the M . This is because the Ca and M are the most influential dimensionless parameters that
555 govern GCO₂-water core flooding displacement ([Kazemifar et al., 2015](#)). As the Ca increases, the impact
556 of the capillary forces compared to viscous forces decreases. The balance between the viscous forces
557 and capillary forces governs the pore scale drainage displacements ([Heaviside and Black, 1983](#)). The
558 capillary forces are responsible for the trapping of the injected CO₂ ([Akbarabadi and Piri, 2013](#); [Bachu
559 and Shaw, 2003](#)). Thus, decreasing the capillary forces (e.g. due to the reduction in the interfacial
560 tension) will lower the S_{wr} (i.e. enhance the fluid displacements) ([Ahmadi et al., 2015](#)). On the other
561 hand, reducing M will result in a more uniform displacement of water by CO₂ ([Bennion and Bachu,
562 2006](#)), which can result in reducing the S_{wr} . The data from [Table 1](#) show that the increase in the Ca and
563 the reduction in the M can lead to a reduction in the S_{wr} even when the change in both Ca and M is
564 small. Ding and Kantzas observed that the critical Ca for the gas-water system is 2E-8 ([Ding and
565 Kantzas, 2007](#)).

566 The results from [Table 1](#) reveal that increasing the fluid pressure from 40 to 70 bar at 33 °C and 0.4
567 ml/min caused the $K_{rCO_2}^{max}$ to increase by around 0.099 and the S_{wr} to decrease by around 0.047. The
568 largest increase in the $K_{rCO_2}^{max}$ and the highest reduction in the S_{wr} occurred as the fluid pressure
569 increased from low-fluid pressure displacements (40 and 50 bar) to high-fluid pressure displacements
570 (70 bar). The observed trend of the $K_{rCO_2}^{max}$ and S_{wr} are in agreement with the findings of Liu et al. and
571 Bennion and Bachu ([Bennion and Bachu, 2006](#); [Liu et al.](#)). Liu et al also observed an increase in the K_{rCO_2}
572 with increasing pressure ([Liu et al.](#)). Bennion and Bachu observed an increase in the K_{rCO_2} and increase
573 in the maximum endpoint CO₂ saturation (i.e. decrease in S_{wr}) with increasing pressure; they attributed

574 that to the reduction in IFT with increasing pressure ([Bennion and Bachu, 2006](#)). The observed trend of
575 the $K_{rCO_2}^{max}$ and S_{wr} can also be associated with the relatively high increase in the Ca and the high
576 reduction in the M .

577 The results from [Table 1](#) reveal that increasing temperature led to an increase in the $K_{rCO_2}^{max}$. On
578 the other hand, increasing temperature caused a reduction in the S_{wr} for the displacements conducted
579 at high-fluid pressure (70 bar) and over a high temperature increase (33-45 °C). Nonetheless, for the
580 experiments conducted at low-fluid pressure (50 bar) and over a small temperature increase (29-33 °C),
581 the trend of the S_{wr} depends on the magnitude of the experimental temperature. For the high-fluid
582 pressure displacements, when the temperature increased from 33 to 45 °C at 70 bar, the $K_{rCO_2}^{max}$
583 increased by around 0.035 and the S_{wr} decreased by around 0.02. The reduction in the S_{wr} for the 70 bar
584 displacements can be attributed also to the high increase in the Ca and the high reduction in the M . For
585 the low-fluid pressure displacements, as the temperature increased slightly from 29 to 33 °C at 50 bar,
586 the $K_{rCO_2}^{max}$ increased by around 0.016. Nevertheless, the S_{wr} value was between around 0.40 and 0.41.
587 The S_{wr} saturation slightly increased by around 0.01 as the temperature increased from 29 to 31 °C, and
588 then slightly decreased by about 0.005 as the temperature increased from 31 to 33 °C. The slight increase
589 in the S_{wr} might be related to the slight reduction in the Ca as well as the impact of the capillary forces,
590 which can be seen through the appearance of the PD oscillations when the temperature increased to 31
591 °C, see Section 3.2 for more information; the PD oscillations might result in hindering water production
592 to a slight extent. On the other hand, the slight reduction in the S_{wr} , when the temperature further
593 increased to 33 °C, can be associated with the relatively high increase in the Ca as well as the slight
594 reduction in the M .

595 Overall, the results from [Table 1](#) shows that the increase in the CO₂ injection rate caused an increase
596 in the $K_{rCO_2}^{max}$ and a reduction in the S_{wr} . Increasing the injection rate from 0.1 to 2 ml/min at 40 bar and
597 33 °C resulted in an increase in the $K_{rCO_2}^{max}$ by around 0.157 and a reduction in the S_{wr} by around 0.05.
598 These findings agree with those in Chang et al. and Akbarabadi and Piri ([Akbarabadi and Piri; Chang](#)

599 [et al., 2013](#)). However, for the core flooding at 0.4 ml/min or less, the S_{wr} trend is not clear. Moreover,
600 the $K_{rCO_2}^{max}$ of the experiments conducted at 40 bar-0.2 ml-33 °C does not fit linearly in the trend.
601 Increasing the injection rate from 0.6 to 1 ml/min resulted in the highest reduction in the S_{wr} . This can
602 be corresponded to the high increase in the Ca from around 7.9 E-8 to 1.3 E-7. For the core flooding
603 performed at 70 bar and 33 °C, increasing the injection rate from 0.2 to 1 ml/min caused a very slight
604 reduction in the S_{wr} by 0.0077. However, the $K_{rCO_2}^{max}$ increased substantially as the injection rate
605 increased from 0.2 to 0.4 ml/min. Nevertheless, as the injection rate increased to 1 ml/min, a significant
606 reduction in the $K_{rCO_2}^{max}$ happened again, the reason is not clear. The very slight reduction in the S_{wr}
607 might be because only a slight increase occurred in the Ca and that M was constant.

608 **Table 1:** Effect of fluid pressure, temperature, and injection rate on endpoint effective and relative
609 permeabilities of gaseous CO₂ and irreducible water saturation

Parameter	Experiment	K_{rCO_2}	K_{rCO_2}	S_{wr}	M	Ca
Fluid Pressure Effect	40 bar-0.4 ml/min-33 °C	1.768	0.113	0.4244	46.26	5.265E-08
	50 bar-0.4 ml/min-33 °C	1.987	0.127	0.4089	44.56	6.250E-08
	70 bar-0.4 ml/min-33 °C	2.613	0.212	0.3779	36.10	2.504E-07
Temperature Effect	50 bar-0.4 ml/min-29 °C	1.507	0.096	0.4012	48.69	4.748E-08
	50 bar-0.4 ml/min-31 °C	1.738	0.111	0.4147	46.57	4.698E-08
	50 bar-0.4 ml/min-33 °C	1.987	0.127	0.4089	44.56	6.250E-08
	70 bar-0.4 ml/min-33 °C	2.613	0.212	0.3779	36.10	2.547E-07
	70 bar-0.4 ml/min-45 °C	3.675	0.247	0.3566	31.34	2.714E-07
Injection Rate Effect	40 bar-0.1 ml/min-33 °C	0.67	0.043	0.38	46.26	1.316E-08
	40 bar-0.2 ml/min-33 °C	1.265	0.081	0.446	46.26	2.632E-08
	40 bar-0.3 ml/min-33 °C	0.955	0.061	0.436	46.26	3.948E-08
	40 bar-0.4 ml/min-33 °C	1.493	0.095	0.4244	46.26	5.265E-08
	40 bar-0.5 ml/min-33 °C	1.528	0.097	0.436	46.26	6.581E-08
	40 bar-0.6 ml/min-33 °C	1.535	0.098	0.4167	46.26	7.897E-08
	40 bar-1 ml/min-33 °C	1.793	0.114	0.3837	46.26	1.316E-07

40 bar-2 ml/min-33 °C	3.13	0.20	0.391	46.26	2.632E-07
70 bar-0.2 ml/min-33 °C	2.421	0.154	0.3798	36.10	1.273E-07
70 bar-0.4 ml/min-33 °C	3.625	0.167	0.3779	36.10	2.547E-07
70 bar-1 ml/min-33 °C	1.976	0.128	0.3721	36.10	6.368E-07

610 4. Conclusion

611 In this paper, the effect of fluid pressure, temperature, and CO₂ injection rate on gaseous CO₂
612 dynamic behaviour during its flooding of a water-saturated sandstone core sample have been
613 investigated in detail. The results indicate that the parameters investigated have a moderate to
614 significant influence on the differential pressure profile, endpoint CO₂ relative and effective
615 permeabilities and irreducible water saturation.

616 For all fluid pressures, temperatures, and injection rates, the differential pressure profiles are
617 characterized by a sharp increase, immediately followed by a steep pressure reduction, and finally, by
618 a gradual pressure reduction. The differential pressure profiles are controlled by the interplay of both
619 capillary and viscous forces. The capillary forces produce cyclic oscillations within the differential
620 pressure and fluid production data; the increase in the viscous forces impede the appearance of these
621 oscillations. The appearance and frequency of the oscillations depend on the fluid pressure,
622 temperature, and CO₂ injection rates. In general, the frequency of the oscillations increased with
623 increasing pressure and temperature. The differential pressure oscillation cycles exhibit a very
624 interesting response to varying injection rate, they are dependent on the fluid pressure. At 40 bar, the
625 oscillations were only observed at an injection rate of 0.4 ml/min, whereas at 70 bar the oscillations
626 occurred at all injection rates tested (0.2, 0.4, and 1ml/min).

627 In general, the increase in fluid pressure, temperature, and injection rate led to an increase in the
628 maximum and quasi-differential pressures; the extent of the increase in the differential pressure is
629 dependent on the fluid pressure, temperature, and injection rate. Increasing the fluid pressure and
630 temperature caused a reduction in the time required to achieve the maximum-differential pressure at

631 the start of the experiment, i.e. corresponding time. Whereas, increasing the injection rate caused the
632 corresponding time to decrease at low injection rates and increase at high injection rates.

633 In general, the increase in fluid pressure, temperature, and injection rate led to an increase in the
634 endpoint CO₂ relative permeability ($K_{rCO_2}^{max}$) and a decline in the irreducible water saturation (S_{wr}). The
635 S_{wr} was in the range of around 0.38-0.45 while the $K_{rCO_2}^{max}$ was less than 0.25.

636 **Acknowledgements:** The authors wish to thank the Higher Committee for Education
637 Development in Iraq and the Ministry of Oil in Iraq for their sponsorship of the first author PhD study.

638 4 References

- 639 Aggelopoulos, C., Robin, M., Perfetti, E., Vizika, O., 2010. CO₂/CaCl₂ solution interfacial tensions under
640 CO₂ geological storage conditions: influence of cation valence on interfacial tension. *Advances in Water*
641 *Resources* 33, 691-697.
- 642 Ahmadi, M.A., Hasanvand, M.z., Behbahani, S.S., Nourmohammad, A., Vahidi, A., Amiri, M., Ahmadi,
643 G., 2015. Effect of operational parameters on the performance of carbonated water injection:
644 Experimental and numerical modeling study. *The Journal of Supercritical Fluids*.
- 645 Akbarabadi, M., Piri, M., Geologic storage of carbon dioxide: an experimental study of permanent
646 capillary trapping and relative permeability, In *Proceedings of International Symposium of the Society*
647 *of Core Analysts, Austin, Texas, USA. 18–21 September 2011*, pp. 18-21.
- 648 Akbarabadi, M., Piri, M., 2013. Relative permeability hysteresis and capillary trapping characteristics
649 of supercritical CO₂/brine systems: An experimental study at reservoir conditions. *Advances in Water*
650 *Resources* 52, 190-206.
- 651 Al-Menhali, A., Krevor, S., 2014. Effective wettability measurements of CO₂-brine-sandstone system at
652 different reservoir conditions. *Energy Procedia* 63, 5420-5426.
- 653 Al-Zaidi, E., Nash, J., Fan, X., 2018. Effect of CO₂ phase on its water displacements in a sandstone core
654 sample. *IJGGC* 71, 227-238.
- 655 Alemu, B.L., Aker, E., Soldal, M., Johnsen, Ø., Aagaard, P., 2011. Influence of CO₂ on rock physics
656 properties in typical reservoir rock: a CO₂ flooding experiment of brine saturated sandstone in a CT-
657 scanner. *Energy Procedia* 4, 4379-4386.
- 658 Alkan, H., Cinar, Y., Ülker, E., 2010. Impact of capillary pressure, salinity and in situ conditions on CO₂
659 injection into saline aquifers. *Transport in porous media* 84, 799-819.
- 660 Armstrong, R.T., McClure, J., Berill, M., Rucker, M., Schlüter, S., Berg, S., 2017. Flow Regimes During
661 Immiscible Displacement. *Petrophysics* 58, 10-18.
- 662 Bachu, S., 2000. Sequestration of CO₂ in geological media: criteria and approach for site selection in
663 response to climate change. *Energy conversion and management* 41, 953-970.
- 664 Bachu, S., 2001. Geological sequestration of anthropogenic carbon dioxide: applicability and current
665 issues. *Geological perspectives of global climate change*, 285-303.
- 666 Bachu, S., 2013. Drainage and imbibition CO₂/brine relative permeability curves at in situ conditions
667 for sandstone formations in western Canada. *Energy Procedia* 37, 4428-4436.
- 668 Bachu, S., Bennion, D.B., 2008a. Interfacial tension between CO₂, freshwater, and brine in the range of
669 pressure from (2 to 27) MPa, temperature from (20 to 125)° C, and water salinity from (0 to 334 000) mg-
670 L- 1. *Journal of Chemical & Engineering Data* 54, 765-775.
- 671 Bachu, S., Bennion, D.B., 2008b. Interfacial tension between CO₂, freshwater, and brine in the range of
672 pressure from (2 to 27) MPa, temperature from (20 to 125)° C, and water salinity from (0 to 334 000) mg-
673 L- 1. *Journal of Chemical & Engineering Data* 54, 765-775.

674 Bachu, S., Bennion, D.B., 2009. Dependence of CO₂-brine interfacial tension on aquifer pressure,
675 temperature and water salinity. *Energy Procedia* 1, 3157-3164.

676 Bachu, S., Shaw, J., 2003. Evaluation of the CO₂ Sequestration Capacity in Alberta's Oil and Gas
677 Reservoirs at Depletion and the Effect of Underlying Aquifers. *Journal of Canadian Petroleum*
678 *Technology* 42.

679 Bahralolom, I., Bretz, R., Orr Jr, F., 1988. Experimental investigation of the interaction of phase behavior
680 with microscopic heterogeneity in a CO₂ flood. *SPE reservoir engineering* 3, 662-672.

681 Banerjee, S., Hassenklover, E., Kleijn, J.M., Cohen Stuart, M.A., Leermakers, F.A., 2013. Interfacial
682 Tension and Wettability in Water–Carbon Dioxide Systems: Experiments and Self-consistent Field
683 Modeling. *The Journal of Physical Chemistry B* 117, 8524-8535.

684 Basbug, B., Gumrah, F., Oz, B., 2005. Simulating the Effects of Deep Saline Aquifer Properties on
685 CO₂ Sequestration, Canadian International Petroleum Conference. Petroleum Society of Canada.

686 Bennion, D.B., Bachu, S., The impact of interfacial tension and pore size distribution/capillary pressure
687 character on CO₂ relative permeability at reservoir conditions in CO₂-brine systems, In *Proceedings of*
688 *the SPE/DOE Symposium on Improved Oil Recovery*. Society of Petroleum Engineers: Houston, TX,
689 USA, 2006., Tulsa, OK, USA, 22–26 April 2006.

690 Bennion, D.B., Bachu, S., 2006. Dependence on temperature, pressure, and salinity of the IFT and
691 relative permeability displacement characteristics of CO₂ injected in deep saline aquifers, *SPE Annual*
692 *Technical Conference and Exhibition*. Society of Petroleum Engineers.

693 Berg, S., Oedai, S., Ott, H., 2013. Displacement and mass transfer between saturated and unsaturated
694 CO₂-brine systems in sandstone. *IJGGC* 12, 478-492.

695 Bikkina, P., Wan, J., Kim, Y., Kneafsey, T.J., Tokunaga, T.K., 2016. Influence of wettability and
696 permeability heterogeneity on miscible CO₂ flooding efficiency. *Fuel* 166, 219-226.

697 Bikkina, P.K., 2011. Contact angle measurements of CO₂-water-quartz/calcite systems in the
698 perspective of carbon sequestration. *International Journal of Greenhouse Gas Control* 5, 1259-1271.

699 Busch, A., Müller, N., 2011. Determining CO₂/brine relative permeability and capillary threshold
700 pressures for reservoir rocks and caprocks: Recommendations for development of standard laboratory
701 protocols. *Energy Procedia* 4, 6053-6060.

702 Cao, S.C., Dai, S., Jung, J., 2016. Supercritical CO₂ and brine displacement in geological carbon
703 sequestration: Micromodel and pore network simulation studies. *International Journal of Greenhouse*
704 *Gas Control* 44, 104-114.

705 Chalbaud, C.A., Lombard, J.-M.N., Martin, F., Robin, M., Bertin, H.J., Egermann, P., 2007. Two Phase
706 Flow Properties of Brine-CO₂ Systems in a Carbonate Core: Influence of Wettability on P_c and k_r,
707 *SPE/EAGE Reservoir Characterization and Simulation Conference*. Society of Petroleum Engineers.

708 Chang, C., Zhou, Q., Xia, L., Li, X., Yu, Q., 2013. Dynamic displacement and non-equilibrium
709 dissolution of supercritical CO₂ in low-permeability sandstone: An experimental study. *International*
710 *Journal of Greenhouse Gas Control* 14, 1-14.

711 Chatzis, I., Morrow, N.R., 1984. Correlation of capillary number relationships for sandstone. *Society of*
712 *Petroleum Engineers Journal* 24, 555-562.

713 Chiquet, P., Broseta, D.F., Thibeau, S., Capillary alteration of shaly caprocks by carbon dioxide, In
714 *Proceedings of the SPE Europec/EAGE Annual Conference*. Society of Petroleum Engineers: Houston,
715 TX, USA, 2005., Madrid, Spain, 13–16 June 2005.

716 Chiquet, P., Daridon, J.-L., Broseta, D., Thibeau, S., 2007. CO₂/water interfacial tensions under pressure
717 and temperature conditions of CO₂ geological storage. *Energy Conversion and Management* 48, 736-
718 744.

719 Chukwudeme, E.A., Hamouda, A.A., 2009. Enhanced oil recovery (EOR) by miscible CO₂ and water
720 flooding of asphaltenic and non-asphaltenic oils. *Energies* 2, 714-737.

721 Cinar, Y., Riaz, A., 2014. Carbon dioxide sequestration in saline formations: Part 2—Review of
722 multiphase flow modeling. *Journal of Petroleum Science and Engineering* 124, 381-398.

723 Delshad, M., Wheeler, M.F., Kong, X., 2010. A critical assessment of CO₂ injection strategies in saline
724 aquifers, *SPE Western Regional Meeting*. Society of Petroleum Engineers.

725 Ding, M., Kantzas, A., 2007. Capillary number correlations for gas-liquid systems. *Journal of Canadian*
726 *Petroleum Technology* 46.

727 Duan, Z., Sun, R., 2003. An improved model calculating CO₂ solubility in pure water and aqueous NaCl
728 solutions from 273 to 533 K and from 0 to 2000 bar. *Chemical Geology* 193, 257-271.

729 Edlmann, K., Bensabat, J., Niemi, A., Haszeldine, R., McDermott, C., 2016. Lessons learned from using
730 expert elicitation to identify, assess and rank the potential leakage scenarios at the Heletz pilot CO₂
731 injection site. *International Journal of Greenhouse Gas Control* 49, 473-487.

732 Edlmann, K., Haszeldine, S., McDermott, C., 2013. Experimental investigation into the sealing
733 capability of naturally fractured shale caprocks to supercritical carbon dioxide flow. *Environmental*
734 *earth sciences* 70, 3393-3409.

735 Espinoza, D.N., Santamarina, J.C., 2010. Water - CO₂ - mineral systems: Interfacial tension, contact
736 angle, and diffusion—Implications to CO₂ geological storage. *Water resources research* 46.

737 Farokhpoor, R., Bjørkvik, B.J., Lindeberg, E., Torsæter, O., 2013a. CO₂ Wettability Behavior During CO₂
738 Sequestration in Saline Aquifer-An Experimental Study on Minerals Representing Sandstone and
739 Carbonate. *Energy Procedia* 37, 5339-5351.

740 Farokhpoor, R., Bjørkvik, B.J.A., Lindeberg, E., Torsæter, O., 2013b. Wettability behaviour of CO₂ at
741 storage conditions. *International Journal of Greenhouse Gas Control* 12, 18-25.

742 Fathollahi, A., Rostami, B., 2015. Carbonated water injection: Effects of silica nanoparticles and
743 operating pressure. *Can. J. Chem. Eng* 93, 1949–1956.

744 Frailey, S.M., Grube, J.P., Seyler, B., Finley, R.J., Investigation of liquid CO₂ sequestration and EOR in
745 low temperature oil reservoirs in the Illinois basin, SPE/DOE Symposium on Improved Oil Recovery.
746 Society of Petroleum Engineers: Houston, TX, USA, 2004., Tulsa, OK, USA, 17–21 April 2004.

747 Fulcher Jr, R.A., Ertekin, T., Stahl, C., 1985. Effect of capillary number and its constituents on two-phase
748 relative permeability curves. *Journal of Petroleum Technology* 37, 249-260.

749 Georgiadis, A., Maitland, G., Trusler, J.M., Bismarck, A., 2010. Interfacial tension measurements of the
750 (H₂O+ CO₂) system at elevated pressures and temperatures. *Journal of Chemical & Engineering Data*
751 55, 4168-4175.

752 Gozalpour, F., Ren, S., Tohidi, B., 2005. CO₂ EOR and storage in oil reservoir. *Oil & gas science and*
753 *technology* 60, 537-546.

754 Gunde, A.C., Bera, B., Mitra, S.K., 2010. Investigation of water and CO₂ (carbon dioxide) flooding using
755 micro-CT (micro-computed tomography) images of Berea sandstone core using finite element
756 simulations. *Energy* 35, 5209-5216.

757 Han, F., Busch, A., van Wageningen, N., Yang, J., Liu, Z., Krooss, B.M., 2010. Experimental study of gas
758 and water transport processes in the inter-cleat (matrix) system of coal: anthracite from Qinshui Basin,
759 China. *International Journal of Coal Geology* 81, 128-138.

760 Hangx, S., van der Linden, A., Marcelis, F., Bauer, A., 2013. The effect of CO₂ on the mechanical
761 properties of the captain sandstone: geological storage of CO₂ at the Goldeneye field (UK).
762 *International Journal of Greenhouse Gas Control* 19, 609-619.

763 Heaviside, J., Black, C., 1983. Fundamentals of relative permeability: experimental and theoretical
764 considerations, SPE Annual Technical Conference and Exhibition. Society of Petroleum Engineers.

765 Herring, A.L., Andersson, L., Newell, D., Carey, J., Wildenschild, D., 2014a. Pore-scale observations of
766 supercritical CO₂ drainage in Bentheimer sandstone by synchrotron x-ray imaging. *International*
767 *Journal of Greenhouse Gas Control* 25, 93-101.

768 Herring, A.L., Andersson, L., Newell, D., Carey, J., Wildenschild, D., 2014b. Pore-scale observations of
769 supercritical CO₂ drainage in Bentheimer sandstone by synchrotron x-ray imaging. *International*
770 *Journal of Greenhouse Gas Control* 25, 93-101.

771 Hildenbrand, A., Schlömer, S., Krooss, B., 2002. Gas breakthrough experiments on fine - grained
772 sedimentary rocks. *Geofluids* 2, 3-23.

773 Iglauer, S., Mathew, M.S., Bresme, F., 2012. Molecular dynamics computations of brine-CO₂ interfacial
774 tensions and brine-CO₂-quartz contact angles and their effects on structural and residual trapping
775 mechanisms in carbon geo-sequestration. *J Colloid Interface Sci* 386, 405-414.

776 Islam, A., Chevalier, S., Sassi, M., 2013. Experimental and Numerical Studies of CO₂ Injection Into
777 Water-Saturated Porous Medium: Capillary to Viscous to Fracture Fingering Phenomenon. *Energy*
778 *Procedia* 37, 5511-5519.

779 Jiang, L., Yu, M., Liu, Y., Yang, M., Zhang, Y., Xue, Z., Suekane, T., Song, Y., 2017. Behavior of
780 CO₂/water flow in porous media for CO₂ geological storage. *Magnetic Resonance Imaging* 37, 100-106.

781 Jobard, E., Sterpenich, J., Pironon, J., Corvisier, J., Jouanny, M., Randi, A., 2013. Experimental simulation
782 of the impact of a thermal gradient during geological sequestration of CO₂: The COTAGES experiment.
783 *International Journal of Greenhouse Gas Control* 12, 56-71.

784 Kaveh, N.S., Wolf, K., Ashrafizadeh, S., Rudolph, E., 2012. Effect of coal petrology and pressure on
785 wetting properties of wet coal for CO₂ and flue gas storage. *International Journal of Greenhouse Gas*
786 *Control* 11, S91-S101.

787 Kazemifar, F., Blois, G., Kyritsis, D.C., Christensen, K.T., 2015. Quantifying the flow dynamics of
788 supercritical CO₂-water displacement in a 2D porous micromodel using fluorescent microscopy and
789 microscopic PIV. *Advances in Water Resources*.

790 Krevor, S., Blunt, M.J., Benson, S.M., Pentland, C.H., Reynolds, C., Al-Menhali, A., Niu, B., 2015.
791 Capillary trapping for geologic carbon dioxide storage-From pore scale physics to field scale
792 implications. *International Journal of Greenhouse Gas Control* 40, 221-237.

793 Krevor, S., Pini, R., Benson, S.M., 2013. Measurement of the multiphase flow properties of the CO₂ brine
794 system for carbon sequestration. *Energy Procedia* 37, 4499-4503.

795 Kwelle, S.O., 2017. Experimental studies on resistance to fluid displacement in single pores, School of
796 Engineering, Institute of Material and Process. The University of Edinburgh, Edinburgh, UK, p. 206.

797 Lassen, R.N., Plampin, M., Sakaki, T., Illangasekare, T., Gudbjerg, J., Sonnenborg, T., Jensen, K.H., 2015.
798 Effects of geologic heterogeneity on migration of gaseous CO₂ using laboratory and modeling
799 investigations. *IJGGC* 43, 213-224.

800 Lenormand, R., Touboul, E., Zarcone, C., 1988. Numerical models and experiments on immiscible
801 displacements in porous media. *Journal of Fluid Mechanics* 189, 37-38.

802 Levine, J.S., Matter, J.M., Goldberg, D.S., Lackner, K.S., Supp, M.G., Ramakrishnan, T., 2011. Two phase
803 brine-CO₂ flow experiments in synthetic and natural media. *Energy Procedia* 4, 4347-4353.

804 Li, X., 2015. Experimental Studies on Pore Wetting and Displacement of Fluid by CO₂ in Porous Media.
805 The University of Edinburgh, Edinburgh, UK.

806 Li, X., Boek, E., Maitland, G.C., Trusler, J.P.M., 2012. Interfacial Tension of (Brines + CO₂): (0.864 NaCl
807 + 0.136 KCl) at Temperatures between (298 and 448) K, Pressures between (2 and 50) MPa, and Total
808 Molalities of (1 to 5) mol·kg⁻¹. *Journal of Chemical & Engineering Data* 57, 1078-1088.

809 Liu, N., Ghorpade, S.V., Harris, L., Li, L., Grigg, R.B., Lee, R.L., The effect of pressure and temperature
810 on brine-CO₂ relative permeability and IFT at reservoir conditions, In Proceedings of the SPE Eastern
811 Regional Meeting. Society of Petroleum Engineers: Houston, TX, USA, 2010., Morgantown, WV, USA,
812 13-15 October 2010.

813 Ma, J., Petrilli, D., Manceau, J.-C., Xu, R., Audigane, P., Shu, L., Jiang, P., Le-Nindre, Y.M., 2013. Core
814 scale modelling of CO₂ flowing: identifying key parameters and experiment fitting. *Energy Procedia*
815 37, 5464-5472.

816 Manceau, J.-C., Ma, J., Li, R., Audigane, P., Jiang, P., Xu, R., Tremosa, J., Lerouge, C., 2015. Two - phase
817 flow properties of a sandstone rock for the CO₂/water system: Core - flooding experiments, and focus
818 on impacts of mineralogical changes. *Water Resources Research* 51, 2885-2900.

819 Miocic, J.M., Gilfillan, S.M., Roberts, J.J., Edlmann, K., McDermott, C.I., Haszeldine, R.S., 2016. Controls
820 on CO₂ storage security in natural reservoirs and implications for CO₂ storage site selection.
821 *International Journal of Greenhouse Gas Control* 51, 118-125.

822 Müller, N., 2011. Supercritical CO₂-brine relative permeability experiments in reservoir rocks—
823 Literature review and recommendations. *Transport in porous media* 87, 367-383.

824 Nourpour Aghbash, V., Ahmadi, M., Evaluation of CO₂-EOR and Sequestration in Alaska West Sak
825 Reservoir Using Four-Phase Simulation Model, SPE Western Regional Meeting. Society of Petroleum
826 Engineers: Houston, TX, USA, 2012., Bakersfield, CA, USA, 21-23 March 2012.

827 Nutt, C., 1982. The physical basis of the displacement of oil from porous media by other fluids: a
828 capillary bundle model, *Proceedings of the Royal Society of London A: Mathematical, Physical and*
829 *Engineering Sciences*. The Royal Society, pp. 155-178.

830 Ott, H., de Kloe, K., Marcelis, F., Makurat, A., 2011. Injection of supercritical CO₂ in brine saturated
831 sandstone: pattern formation during salt precipitation. *Energy Procedia* 4, 4425-4432.

832 Ott, H., Pentland, C., Oedai, S., 2015. CO₂-brine displacement in heterogeneous carbonates.
833 *International Journal of Greenhouse Gas Control* 33, 135-144.

834 Peace software, 2017.

835 Pentland, C., El-Maghraby, R., Georgiadis, A., Iglauer, S., Blunt, M., 2011a. Immiscible displacements
836 and capillary trapping in CO₂ storage. *Energy Procedia* 4, 4969-4976.

837 Pentland, C.H., El - Maghraby, R., Iglauer, S., Blunt, M.J., 2011b. Measurements of the capillary
838 trapping of supercritical carbon dioxide in Berea sandstone. *Geophysical Research Letters* 38.

839 Perrin, J.-C., Benson, S., 2010. An experimental study on the influence of sub-core scale heterogeneities
840 on CO₂ distribution in reservoir rocks. *Transport in porous media* 82, 93-109.

841 Perrin, J.-C., Krause, M., Kuo, C.-W., Miljkovic, L., Charoba, E., Benson, S.M., 2009. Core-scale
842 experimental study of relative permeability properties of CO₂ and brine in reservoir rocks. *Energy*
843 *Procedia* 1, 3515-3522.

844 Physics, D.o., 2017. Q & A: Temperature and Water Molecules | Department of Physics | the University
845 of Illinois at Urbana-Champaign.

846 Pini, R., Krevor, S.C., Benson, S.M., 2012. Capillary pressure and heterogeneity for the CO₂/water
847 system in sandstone rocks at reservoir conditions. *Advances in Water Resources* 38, 48-59.

848 Plug, W.-J., Bruining, J., 2007. Capillary pressure for the sand-CO₂-water system under various
849 pressure conditions. Application to CO₂ sequestration. *Advances in Water Resources* 30, 2339-2353.

850 Qi, R., Laforce, T., Blunt, M., 2010. Carbon Dioxide (CO₂) Injection Design to Maximize Underground
851 Reservoir Storage and Enhanced Oil Recovery (EOR). *Developments and Innovation in Carbon Dioxide*
852 *(CO₂) Capture and Storage Technology* (Ed. MM Maroto-Valer), Woodhead Publishing Series in
853 *Energy*, Oxford, 169-184.

854 Rathnaweera, T., Ranjith, P., Perera, M., 2015. Effect of salinity on effective CO₂ permeability in
855 reservoir rock determined by pressure transient methods: An experimental study on Hawkesbury
856 sandstone. *Rock Mechanics and Rock Engineering* 48, 2093-2110.

857 Rezaei, N., Firoozabadi, A., 2014. Pressure evolution and production performance of waterflooding in
858 n-heptane-saturated fired Berea cores. *SPE Journal* 19, 674-686.

859 Roof, J., 1970. Snap-off of oil droplets in water-wet pores. *Society of Petroleum Engineers Journal* 10,
860 85-90.

861 Rostami, B., Kharrat, R., Ghotbi, C., Tabatabaie, S., 2010. Gas-oil relative permeability and residual oil
862 saturation as related to displacement instability and dimensionless numbers. *Oil & Gas Science and*
863 *Technology-*Revue de l'Institut Français du Pétrole** 65, 299-313.

864 Saeedi, A., Rezaee, R., Evans, B., Clennell, B., 2011. Multiphase flow behaviour during CO₂ geo-
865 sequestration: Emphasis on the effect of cyclic CO₂-brine flooding. *Journal of Petroleum Science and*
866 *Engineering* 79, 65-85.

867 Sakurovs, R., Lavrencic, S., 2011. Contact angles in CO₂-water-coal systems at elevated pressures.
868 *International Journal of Coal Geology* 87, 26-32.

869 Salimi, H., Wolf, K.-H., Bruining, J., 2012. The influence of capillary pressure on the phase equilibrium
870 of the CO₂-water system: Application to carbon sequestration combined with geothermal energy.
871 *International Journal of Greenhouse Gas Control* 11, S47-S66.

872 Saraji, S., Goual, L., Piri, M., Plancher, H., 2013. Wettability of supercritical carbon dioxide/water/quartz
873 systems: simultaneous measurement of contact angle and interfacial tension at reservoir conditions.
874 *Langmuir: the ACS journal of surfaces and colloids* 29, 6856-6866.

875 Saraji, S., Piri, M., Goual, L., 2014. The effects of SO₂ contamination, brine salinity, pressure, and
876 temperature on dynamic contact angles and interfacial tension of supercritical CO₂/brine/quartz
877 systems. *International Journal of Greenhouse Gas Control* 28, 147-155.

878 Schembre, J.M., Kovscek, A.R., 2003. A technique for measuring two-phase relative permeability in
879 porous media via X-ray CT measurements. *Journal of Petroleum Science and Engineering* 39, 159-174.
880 Shi, J.-Q., Xue, Z., Durucan, S., 2011. Supercritical CO₂ core flooding and imbibition in Tako
881 sandstone—Influence of sub-core scale heterogeneity. *International Journal of Greenhouse Gas Control*
882 5, 75-87.

883 Skauge, A., Håskjold, G., Thorsen, T., Aarra, M., Accuracy of gas-oil relative permeability from two-
884 phase flow experiments, In *Proceedings of International Symposium of the Society of Core Analysts*,
885 Calgary, AB, Canada, 7–10 September, 1997.

886 Sohrabi, M., Jamiolahmady, M., Al Quraini, A., Heavy Oil Recovery by Liquid CO₂/Water Injection,
887 EUROPEC/EAGE Conference and Exhibition. Society of Petroleum Engineers: Houston, TX, USA, 2007,
888 London, UK 11–14 June 2007.

889 Song, Y., Jiang, L., Liu, Y., Yang, M., Zhao, Y., Zhu, N., Dou, B., Abudula, A., 2012. An experimental
890 study on CO₂/water displacement in porous media using high-resolution magnetic resonance imaging.
891 *International Journal of Greenhouse Gas Control* 10, 501-509.

892 Suekane, T., Soukawa, S., Iwatani, S., Tsushima, S., Hirai, S., 2005. Behavior of supercritical CO₂ injected
893 into porous media containing water. *Energy* 30, 2370-2382.

894 Suenaga, H., Nakagawa, K., 2011. Analysis of two-phase flow properties of sandstones to evaluate their
895 suitability for geologic storage of CO₂. *Energy Procedia* 4, 4323-4330.

896 Trevisan, L., Pini, R., Cihan, A., Birkholzer, J.T., Zhou, Q., González - Nicolás, A., Illangasekare, T.H.,
897 2017. Imaging and quantification of spreading and trapping of carbon dioxide in saline aquifers using
898 meter - scale laboratory experiments. *Water Resources Research* 53, 485-502.

899 Tutolo, B.M., Luhmann, A.J., Kong, X.-Z., Saar, M.O., Seyfried, W.E., 2015. CO₂ sequestration in
900 feldspar-rich sandstone: coupled evolution of fluid chemistry, mineral reaction rates, and
901 hydrogeochemical properties. *Geochimica et Cosmochimica Acta* 160, 132-154.

902 Wang, D., Dong, B., Breen, S., Zhao, M., Qiao, J., Liu, Y., Zhang, Y., Song, Y., 2015. Review: Approaches
903 to research on CO₂/brine two-phase migration in saline aquifers. *Hydrogeology Journal* 23, 1-18.

904 Wang, D., Zhao, M., Song, Y., Xu, H., Ma, X., 2013. Influence of Capillary Pressure and Injection Rate
905 as well as Heterogeneous and Anisotropic Permeability on CO₂ Transport and Displacement Efficiency
906 in Water-Saturated Porous Media. *Energy Procedia* 37, 3945-3951.

907 Xu, R., Luo, S., Jiang, P., 2011. Pore scale numerical simulation of supercritical CO₂ injecting into porous
908 media containing water. *Energy Procedia* 4, 4418-4424.

909 Yang, D., Gu, Y., Tontiwachwuthikul, P., 2007. Wettability determination of the reservoir brine-
910 reservoir rock system with dissolution of CO₂ at high pressures and elevated temperatures. *Energy &*
911 *Fuels* 22, 504-509.

912 Yu, J., Liu, N., Li, L., Lee, R.L., 2012. Generation of nanoparticle-stabilized supercritical CO₂ foams,
913 Carbon Management Technology Conference. Carbon Management Technology Conference.

914 Yu, M., Song, Y., Jiang, L., Li, W., 2014. CO₂/Water Displacement in Porous Medium Under Pressure
915 and Temperature Conditions for Geological Storage. *Energy Procedia* 61, 282-285.

916 Zhang, C., Oostrom, M., Grate, J.W., Wietsma, T.W., Warner, M.G., 2011. Liquid CO₂ Displacement of
917 Water in a Dual-Permeability Pore Network Micromodel. *Environmental science & technology* 45,
918 7581-7588.

919